NASA/TM—2003–212930

Overview of Nonnuclear Testing of the Safe, Affordable 30-kW Fission Engine Including End-to-End Demonstrator Testing

M.K. Van Dyke, J.J. Martin, and M.G. Houts
Marshall Space Flight Center, Marshall Space Flight Center, Alabama

November 2003

The NASA STI Program Office…in Profile

Since its founding, NASA has been dedicated to the advancement of aeronautics and space science. The NASA Scientific and Technical Information (STI) Program Office plays a key part in helping NASA maintain this important role.

The NASA STI Program Office is operated by Langley Research Center, the lead center for NASA's scientific and technical information. The NASA STI Program Office provides access to the NASA STI Database, the largest collection of aeronautical and space science STI in the world. The Program Office is also NASA's institutional mechanism for disseminating the results of its research and development activities. These results are published by NASA in the NASA STI Report Series, which includes the following report types:

- TECHNICAL PUBLICATION. Reports of completed research or a major significant phase of research that present the results of NASA programs and include extensive data or theoretical analysis. Includes compilations of significant scientific and technical data and information deemed to be of continuing reference value. NASA's counterpart of peer-reviewed formal professional papers but has less stringent limitations on manuscript length and extent of graphic presentations.

- TECHNICAL MEMORANDUM. Scientific and technical findings that are preliminary or of specialized interest, e.g., quick release reports, working papers, and bibliographies that contain minimal annotation. Does not contain extensive analysis.

- CONTRACTOR REPORT. Scientific and technical findings by NASA-sponsored contractors and grantees.

- CONFERENCE PUBLICATION. Collected papers from scientific and technical conferences, symposia, seminars, or other meetings sponsored or cosponsored by NASA.

- SPECIAL PUBLICATION. Scientific, technical, or historical information from NASA programs, projects, and mission, often concerned with subjects having substantial public interest.

- TECHNICAL TRANSLATION. English-language translations of foreign scientific and technical material pertinent to NASA's mission.

Specialized services that complement the STI Program Office's diverse offerings include creating custom thesauri, building customized databases, organizing and publishing research results…even providing videos.

For more information about the NASA STI Program Office, see the following:

- Access the NASA STI Program Home Page at ***http://www.sti.nasa.gov***

- E-mail your question via the Internet to help@sti.nasa.gov

- Fax your question to the NASA Access Help Desk at (301) 621–0134

- Telephone the NASA Access Help Desk at (301) 621–0390

- Write to:
  NASA Access Help Desk
  NASA Center for AeroSpace Information
  7121 Standard Drive
  Hanover, MD 21076–1320
  (301)621–0390

NASA/TM—2003–212930

Overview of Nonnuclear Testing of the Safe, Affordable 30-kW Fission Engine, Including End-to-End Demonstrator Testing

M.K. Van Dyke, J.J. Martin, and M.G. Houts
Marshall Space Flight Center, Marshall Space Flight Center, Alabama

National Aeronautics and
Space Administration

Marshall Space Flight Center • MSFC, Alabama 35812

November 2003

TRADEMARKS

Trade names and trademarks are used in this report for identification only. This usage does not constitute an official endorsement, either expressed or implied, by the National Aeronautics and Space Administration.

Available from:

NASA Center for AeroSpace Information
7121 Standard Drive
Hanover, MD 21076–1320
(301) 621–0390

National Technical Information Service
5285 Port Royal Road
Springfield, VA 22161
(703) 487–4650

TABLE OF CONTENTS

LIST OF FIGURES

LIST OF FIGURES (Continued)

LIST OF FIGURES (Continued)

LIST OF TABLES

LIST OF ACRONYMS AND SYMBOLS

ac	alternating current
Ar	argon
BeO	beryllium oxide
C	carbon
CDDF	Center Director's Discretionary Fund
CO_2	carbon dioxide
Cu	copper
DAQ	data acquisition and control
dc	direct current
DOE	Department of Energy
ds	downstream
GHe	gaseous helium
He	helium
HED	heat exchanger design
HH	heater head
HIP	hot isostatic pressing
HP	heat pipe
HPS	heat pipe power system
HPSMARS	heat pipe power system Mars
HX	heat exchanger
ID	inside diameter

LIST OF ACRONYMS AND SYMBOLS (Continued)

IGBT	insulated gate bipolar transistor
JPL	Jet Propulsion Laboratory
K	potassium
LANL	Los Alamos National Laboratory
Li	lithium
MCNP	Monte Carlo neutral particle (transport code)
Mo	molybdenum
MSFC	Marshall Space Flight Center
MUTT	module unfueled thermohydraulic test
Na	sodium
NEP	nuclear-electric propulsion
NI	National Instruments Corporation
Ni	nickel
NSTAR	NASA Solar Electric Propulsion Technology Application Readiness
OD	outside diameter
PIE	post-irradiation examination
PRC	Propulsion Research Center
RF	radio frequency
SAFE–30	safe, affordable 30-kW fission engine
SCXI	signal conditioning extensions for instrumentation
SNAP	systems for nuclear auxiliary power
SP–100	space power 100 (system)
SPAR	space power advance reactor

LIST OF ACRONYMS AND SYMBOLS (Continued)

SPUR	Sandia pulsed uranium reactor
SS	stainless steel
TC	thermocouple
TFE	thermionic fuel element
TFEVP	thermionic fuel element verification program
TIG	tungsten inert gas
TM	Technical Memorandum
U	uranium
UN	uranium nitride
UO_2	uranium dioxide
U.S.	United States
us	upstream

NOMENCLATURE

A	surface area
A_{CH}	surface area of cartridge heater
A_{FT}	surface area of fuel tube
$\vec{B}$	magnetic field
c_p	heat capacity
$c_{p,CH}$	heat capacity of cartridge heater
$c_{p,FT}$	heat capacity of fuel tube
d_o	heat pipe outside diameter
I	current
i	index used to describe conditions of a variable
$\dot{m}$	mass flow rate of calorimeter cooling water
m_{CH}	mass of cartridge heater
m_{FT}	mass of fuel tube
N_C	total number of condenser segments
P	power
p	perimeter
Q	power
Q_{tube}	heat flux or power from individual heater tube
$Q_{\text{total\_input}}$	total heat flux or power into the SAFE–30 core
q	heat transfer rate
$q_{\text{condenser}}$	heat transfer rate (radiant) between heat pipe condenser surface and its surroundings
$q_{\text{electrical}}$	heat transfer rate between the cartridge heater and its surroundings
$q_{\text{evaporator}}$	heat transfer rate from fuel tubes to evaporator

NOMENCLATURE (Continued)

T	temperature
T_{CH}	temperature of cartridge heater
T_{FT}	temperature of fuel tube
T_{heaters}	temperature of heaters
T_{tube}	temperature of tube
T_i	temperature at $t=i$
T_∞	temperature of surroundings
t	time
V	voltage
V_+	beam voltage
V_-	acceleration grid voltage
V_D	discharge voltage
z	axial position
z_i	axial position at $z=i$
ΔT	temperature difference
ε	emissivity
ε_{CH}	emissivity of cartridge heater
ε_{FT}	emissivity of fuel tube
σ	Stefan-Boltzmann constant

TECHNICAL MEMORANDUM

OVERVIEW OF NONNUCLEAR TESTING OF THE SAFE, AFFORDABLE 30-kW FISSION ENGINE, INCLUDING END-TO-END DEMONSTRATOR TESTING

1. INTRODUCTION AND PROGRAM DESCRIPTION

1.1 Identifying the Need for Nonnuclear Testing

The discovery of fission was reported in February 1939. On December 2, 1942, the world's first self-sustaining fission chain was realized at The University of Chicago. Fission reactors have since been used extensively by the United States (U.S.) Navy (powering submarines and surface ships) and the commercial power industry. Twenty percent of U.S. electricity is provided by fission reactors, and the percentage is much higher in other countries. Operating experience in the United States alone totals thousands of reactor years.

The potential for using space fission systems to open the solar system to extensive exploration, development, and settlement has been recognized for decades. However, despite numerous U.S. programs aimed at developing and utilizing fission systems, the only U.S. flight of a fission system occurred over three decades ago on April 3, 1965 (SNAP 10A). Although the Former Soviet Union successfully utilized over 30 fission systems in space, all U.S. programs since 1965 have failed to fly. Table 1 is a partial list of the major U.S. space fission programs which have failed to result in a flight system.

Table 1. Partial list of major U.S. space fission programs that have failed to result in flight of a system.

• Solid-Core Nuclear Rocket Program	• SNAP–50/SPUR	• Advanced Liquid Metal-Cooled Reactor
• Medium-Power Reactor Experiment	• High-Temperature Gas-Cooled Electric Power Reactor (710 Reactor)	• Advanced Space Nuclear Power Program
• Thermionic Technology Program (1963–1973)	• SPAR/SP–100	• Multi-Megawatt Program
• Space Nuclear Thermal Rocket Program	• Flight Topaz	• Thermionic Fuel Element Verification Program
• SP–100	• DOE 40 kW_e Thermionic Reactor Program	• Air Force Bimodal Study

Previous space fission system development programs have failed for a variety of reasons. It is clear, however, that improvements need to be made both technically and programmatically in order to succeed with current attempts to field a space fission system. Heavy reliance on nuclear testing increases cost and makes it very difficult to achieve significant milestones early in a program. A potential way to improve programs is to design systems that allow maximum benefit from realistic nonnuclear testing.

Successful development of space fission systems will require an extensive program of affordable and realistic testing. In addition to tests related to design/development of the fission system, realistic testing of the actual flight unit must also be performed. Testing can be divided into two categories—nonnuclear tests and nuclear tests.

Full-power nuclear tests of space fission systems are expensive, time consuming, and of limited use, even in the best of programmatic environments. Factors to consider when performing nuclear tests include the following:

(1) Time and cost associated with fabricating and handling the test article.

(2) Nonflight-prototypic modifications to the test article required to enable ground testing.

(3) Required modifications to existing nuclear facilities to enable testing.

(4) Time and cost associated with testing the article at a nuclear facility.

(5) Time and cost associated with radiological cooldown and transfer/shipping to a hot cell.

(6) Expense and slow pace of assessing failures in a hot cell environment.

(7) Limited ability to correctly identify failure mechanisms in a hot cell environment.

History provides examples. During the highly successful Rover Nuclear Rocket Development Program, it still took nearly 4 yr to move from the 1968 Pewee ground nuclear test to the follow-on nuclear test, the Nuclear Furnace 1 test in 1972. The first five full ground nuclear power tests of the program (Kiwi A, Kiwi A , Kiwi A3, Kiwi B1A, and Kiwi B1B; total cost: >$1B FY 2000 equivalent) all resulted in massive fuel damage due to thermal hydraulic problems and flow-induced vibrations. These problems were not resolved until nonnuclear cold-flow tests were performed. During the SP–100 program, tens of millions of dollars were spent attempting to modify the Hanford site 309 building to allow a full ground nuclear test of an SP–100 system. In addition, the system to be tested (SP–100 ground engineering system) was significantly different from the SP–100 generic flight system. The Hanford site 309 building was selected in 1985 to be the site of the ground engineering system test. At the end of the SP–100 program, nearly 10 yr later, significant modifications still remained before nuclear tests could be performed in the building. During the thermionic fuel element (TFE) verification program (TFEVP), it frequently took more than a year for TFEs and TFE components to be removed from the test reactor, shipped, and readied for postirradiation examination (PIE). When PIE was performed, limited data were obtained due to the expense, time, and limited equipment availability associated with working in a hot cell. The Rover program, the SP–100 program, and the TFEVP never led to the flight of a space fission system.

If fission systems are to be utilized for any flight program in the United States, the next fission flight system must be safe, simple, robust, and inexpensive to develop. Technology risks must be kept at a minimum, development and utilization should be inexpensive and timely, and the experience from existing nuclear databases should be utilized. This would mean that no new nuclear development would be required for full confidence in a flight demonstrator; thus, development challenges, if any, would be related to thermal hydraulics, structures, and "balance of plant."

Because heat from fission cannot be used for full-power testing of flight units due to radiological activation, space fission systems must be designed such that heat from fission can be very closely mimicked by some other means. While some nuclear testing will be required, ideally the system will be optimized to allow maximum benefit from nonnuclear testing during the development phase. Nonnuclear tests are affordable and timely, and the cause of component and system failures can be quickly and accurately identified. The primary concern with nonnuclear tests is that nuclear effects are obviously not taken into account. To be most relevant, the system undergoing nonnuclear tests must thus be designed to operate well within established radiation damage and fuel burnup limits. In addition, the system must be designed such that minimal assembly is required to move from nonnuclear testing mode to a fueled system operating on heat from fission. If the system is designed to operate within established radiation damage and fuel burnup limits while simultaneously allowing close simulation of heat from fission using resistance heaters, high confidence in fission system performance and lifetime can be attained through a series of nonnuclear tests. Any subsequent operation of the system using heat from fission instead of resistance heaters would then be viewed much more as a demonstration than a test; i.e., the probability of system failure would be very low. Required nuclear performance data could be obtained from warm and cold zero-power critical testing and dimensional changes measured during nonnuclear testing.

Benefits of a strong nonnuclear ground test program include, but are not limited to the following:

- Nonnuclear ground tests are directly applicable to nuclear system development.
- Technology issues can be demonstrated/resolved faster and cheaper with a combination of ground-based hardware testing and paper studies rather than paper studies alone.
- Program success does not hinge on performing nuclear testing. Issues can be resolved and program paybacks can be discovered long before a nuclear test has to be performed.
- Robustness of the system can be demonstrated. This results in high confidence in the probability of flight success.
- "What if" questions can be answered quickly and inexpensively.
- Realistic margins of safety can be established through failure testing with no "nuclear" issues involved.
- Significant yearly milestones can be achieved within modest budgets and schedules, breaking the cycle of endless paper studies.

- Significant technical progress can be made with minimal risk of being eliminated politically.
- Extensive tests can be performed on an actual flight unit.
- Testing provides a mechanism to test and prove several concepts under consideration inexpensively and quickly, and enables an informed downselect.
- The field of concepts for consideration are narrowed down early in the program. If the system is not easily nonnuclear testable, the system will only inflate in developmental cost.
- Intrasystem, intersystem, and item interfaces are identified.
- Major integration issues are identified early and the impact of one system parameter on another is determined.
- The completeness of system performance and design requirements allocated for the detailed design are confirmed and assured.
- Performance and physical design characteristics are verified. This information feeds back into the design of the systems. It is much less expensive to incorporate the design change early in the program rather than later.
- Information pertinent to actual system characteristics can be derived and used as input to the overall system evaluation and assessment.
- Bench testing now provides inputs to thermal and structural models that will be used later to either design or verify the systems.
- A general technology and evolutionary path to follow are provided rather than waiting for specific program direction 8 yr down the road.
- The test bed would be evolved into the advanced design and development phase quickly and cheaply since the expertise for this type of testing would already exist.
- Success probability of a full-power ground nuclear test is increased, if such a test is deemed cost effective.

All future space fission system development programs could benefit from optimizing the use of realistic nonnuclear tests. First-generation systems will benefit the most, as they are most likely to operate within established radiation damage and fuel burnup limits. While some nuclear testing may be required, ideally the system will be optimized to allow maximum benefit from nonnuclear testing during the development phase. Although advanced fission systems will require extensive nuclear testing, experience and support gained from the in-space utilization of earlier systems should facilitate their development.

1.2 Phase 1 Fission Systems

At the power levels under consideration (3 to 300 kW electric power), almost all technical issues are thermal or stress related, and will not be strongly affected by the radiation environment. These issues can be resolved more thoroughly, less expensively, and in a more timely fashion compared to nuclear testing, provided the nonnuclear testing is prototypic of the system in question. Phase 1 systems are defined as those with a thermal power level of ≤1.5 MW and are designed to operate within established radiation damage and fuel burnup limits, while simultaneously being designed to allow close simulation of heat from fission using resistance heaters. High confidence in fission system performance and lifetime can be attained through a series of nonnuclear tests. Additionally, phase 1 systems deliver thermal energy to the power conversion subsystem at temperatures up to 1,300 K.

1.3 A Stepwise Approach to Achieving Nonnuclear Testing of Nuclear Systems Capability for Heat Pipe Reactor Systems

In order to achieve the maximum benefits of a strong nonnuclear testing program, tangible realistic prototypic hardware milestones must be shown on a yearly basis. Additionally, each product must build on the success of its predecessor and must be applicable to the next system. This approach was used for the safe, affordable fission engine (SAFE) test article development program and accomplished via cooperative efforts with Department of Energy (DOE) labs, industry, universities, and other NASA Centers. Through hardware-based design and testing, the SAFE program investigates component, subsystem, and integrated design and performance. While this approach is being adapted for all reactor concepts tested at Marshall Space Flight Center (MSFC), this Technical Memorandum (TM) addresses the SAFE series, specifically, the SAFE–30 test article only. Figure 1 shows the SAFE series of nonnuclear test programs that ultimately leads to the nonnuclear demonstration of a 400-kW (refractory metal core) flight configuration system. Follow-on work could involve design, development, and testing of a 1,000-kW or higher system.

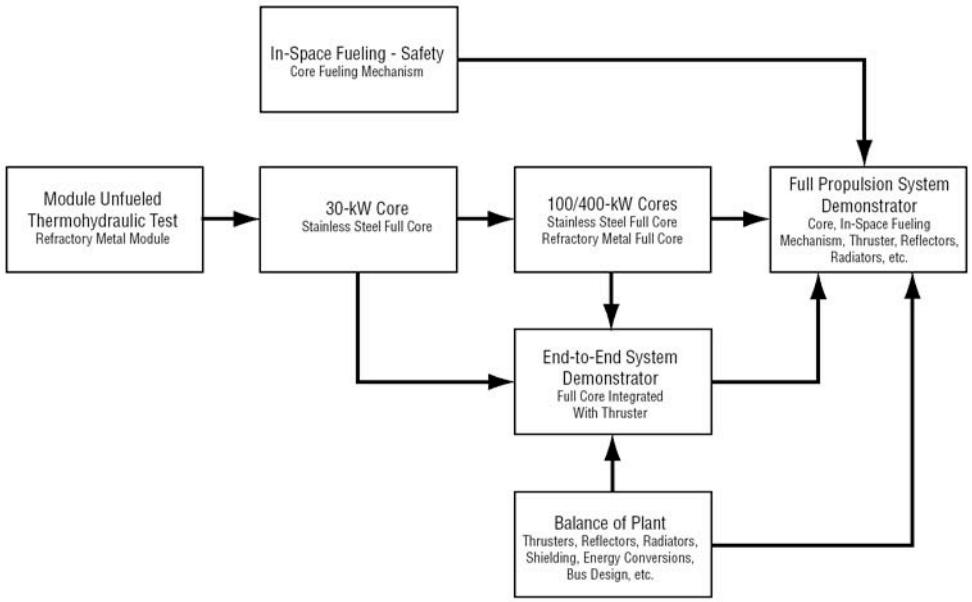

Figure 1. The SAFE test program.

The purpose of the first module unfueled thermohydraulic test (MUTT) series was to verify that the heat from fission could be realistically mimicked using resistance heaters. The heat from fission was then utilized by transport through a heat pipe and by direct transport to helium (He) (which simulated hydrogen propellant). The second test series, SAFE–30, was a full-core test capable of operating at 30-kW thermal power, again using resistance heating to simulate the heat from fission. This core contained 48 "fuel pins" or heaters and 12 stainless steel/sodium (Na) heat pipes. Heat was carried out of the core via heat pipes. The third test series, the end-to-end system demonstrator, used the SAFE–30 core in combination with a Stirling engine manufactured by Stirling Technology Company of Kennewick, WA, and an electric propulsion engine to perform a full nuclear-electric propulsion (NEP) system demonstration, the first of its kind in the United States. The fourth test series, SAFE–100, is similar to the SAFE–30 test series; however, this series uses a smaller pin geometry more closely resembling a flight-like configuration. The fifth test series, SAFE–400, is a refractory metal core and is representative of a flight-like configuration for an NEP system requiring 400 kW thermal power to support 100 kW of electrical power conversion. This TM will give a brief background discussion on the MUTT series before describing the SAFE–30 series and the end-to-end demonstrator.

1.4 Previous Nonnuclear Testing Results

The MUTT series was performed in 1998 and 1999 at MSFC. The MUTT (fig. 2) was a 5.08-cm-diameter, 45-cm-long pure tungsten (W) "block," representing a module with six fuel pins surrounding a central molybdenum- (Mo-) lithium (Li) heat pipe. The W block, heated with six resistance heaters to simulate the heat produced by nuclear fuel elements, reached a peak temperature of 2,100 K. Representative interstitial holes were oriented parallel to the fuel pins and provided for direct thermal heating of injected gases, simulating nuclear thermal rocket operation. Typically, gaseous helium (GHe) was passing through the module for direct heating simulations. A Mo-Li heat pipe, developed at Los Alamos National Laboratory (LANL), was inserted into the center hole of the W block and supported at the free end by a stainless steel support bar. The heat pipe has a length of 145 cm, an outside diameter (OD) of 1.27 cm, and is equipped with a crescent-annular wick structure consisting of seven layers of sintered Mo screen (400 mesh). Before delivery to MSFC, the heat pipe was tested at LANL where it was operated in a radiation-coupled environment transferring 1 kW at 1,450 K. Figure 2 shows the W block with the heat pipe, resistance heaters, and gas entrance. Figure 3 shows the heat pipe assembly in a vacuum chamber.

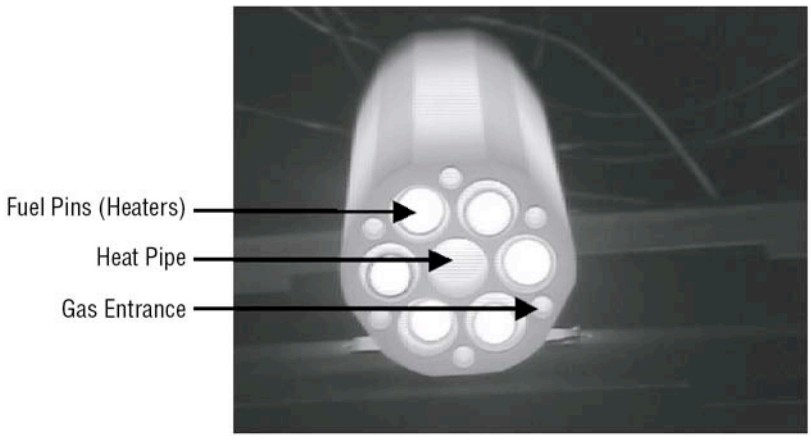

Figure 2. Position of heat pipe, heaters, and gas entrance on MUTT.

Figure 3. Instrumented Mo-Li heat pipe.

The MUTT series has five top-level goals:

(1) Demonstrate that realistic nonnuclear testing can be used to resolve thermal hydraulic and other issues associated with space fission system development.

(2) Demonstrate that the eventual user of space fission systems—in this case, NASA—can be heavily involved in all aspects of space fission system development.

(3) Demonstrate the desirability of a modular core design that allows issues to be resolved on a module level prior to fabrication and testing of a full core.

(4) Demonstrate the superiority of hardware-based technology assessment over the never-ending cycle of paper studies often associated with advanced system development.

(5) Experience gained from the MUTT series will be directly applicable to full-core tests slated to begin in late FY2002.

Specific technical goals of the MUTT series include:

(1) Gain experience using resistance heaters to realistically simulate heat from fission. Test module to thermal design limits by demonstrating capability of module to operate at 1,477 °C (1,750 K).

(2) Demonstrate energy transfer capability of the heat pipe (>1 kW). Test heat pipe to thermal design limits by demonstrating an operating temperature of 1,027 °C (1,300 K).

(3) Demonstrate heat pipe operation at extreme transients (fast start followed by instantaneous shutdown).

(4) Demonstrate direct thermal propulsion by introduction of cold gas (ambient conditions) and extraction of hot gas (900 °C) from the chamber.

(5) Development of instrumentation techniques for flow, temperature, and other measurements in a simulated fission system.

High-temperature boron nitride heaters, capable of exceeding 2,000 K, were designed and produced by Advanced Ceramics, Inc., of Lakewood, OH. They were connected in two heater pairs which were connected in parallel to an electrical feedthrough. Fourteen-gauge copper (Cu) wires connected the heaters via the feedthrough. This provided the MUTT with a maximum available power of 3 kW to each heater. Digital output multimeters delivered total heater current and voltage information to the data acquisition system. Temperature readings were obtained with an optical pyrometer and thermocouples.

The heat pipe was instrumented with nine type C thermocouples tack welded to the heat pipe on a nickel (Ni) foil interlayer. The distance between the first eight thermocouples was ≈10 cm and began 10 cm from the end of the block. The distance between the last two thermocouples was ≈20 cm. One thermocouple was attached to the W block and one thermocouple was attached to the vacuum chamber wall. An optical pyrometer was used to verify the accuracy of the thermocouple data. The thermocouple temperature data were recorded by the data acquisition system.

GHe is injected through a gas feedthrough to a manifold that distributes the gas into six feeds that connect to the inlet side end cap of the W block. The gas is then heated by the block and vented into the chamber where it is pumped out by the vacuum system. The exhaust end cap is outfitted with thermocouples positioned over the gas exhaust holes to record change in temperature. Inlet temperature of the gas is measured prior to injection into the chamber. Gas flow rate is monitored and controlled by an MKS Instruments, Inc., flow control unit. Temperature and pressure measurements were then used to predict module performance if operating in the thermal rocket mode.

Pressure in the chamber was monitored using multiple vacuum thermocouple gauges for pressures $>10^{-3}$ torr. For pressures below the capability of the thermocouple gauge, a cold cathode and Bayard-Albert ion gauge were used. Real-time pressure data were gathered both by a stand-alone Varian vacuum multigauge controller and National Instruments™ (NI) LabVIEW™.

LabVIEW software and corresponding NI hardware was selected as the data acquisition and control (DAQ) system due to its high level of industry implementation and versatility. LabVIEW is highly modular and has been customized to perform most routine operations standard to the propellant energy source test bed. The DAQ hardware consisted of an NI signal conditioning extensions for instrumentation (SCXI) chassis outfitted with cards specific to MUTT needs. The chassis contained a

thermocouple card, a control card for operation of valves and switches, and a card to handle the pressure information. The SCXI chassis was connected to a computer running LabVIEW software, collecting and assembling test data as well as monitoring most aspects of the experiment. All electronic controls and data acquisition devices were located on a rack next to the chamber.

The first test determined the ability of the heaters to heat the module; neither gas flow nor a heat pipe were included in this test. The heaters were set at a constant power level and the uninsulated module temperature was recorded using an optical pyrometer. The power level was kept at a constant level until the module temperature reached a steady-state condition. The terminal voltage across each heater was then increased by 20 V and kept at a constant level until the module again reached steady state. This procedure continued until the maximum available current that could be delivered by the power supply was reached. This corresponded to a maximum power of ≈7 kW delivered to the heaters and a module maximum temperature of 1,663 K. Figure 4 shows the time-temperature profile for this test. Although the curved shape is similar for each power level, at higher power levels (temperatures), the module temperature had a larger slope and reached steady state fairly quickly.

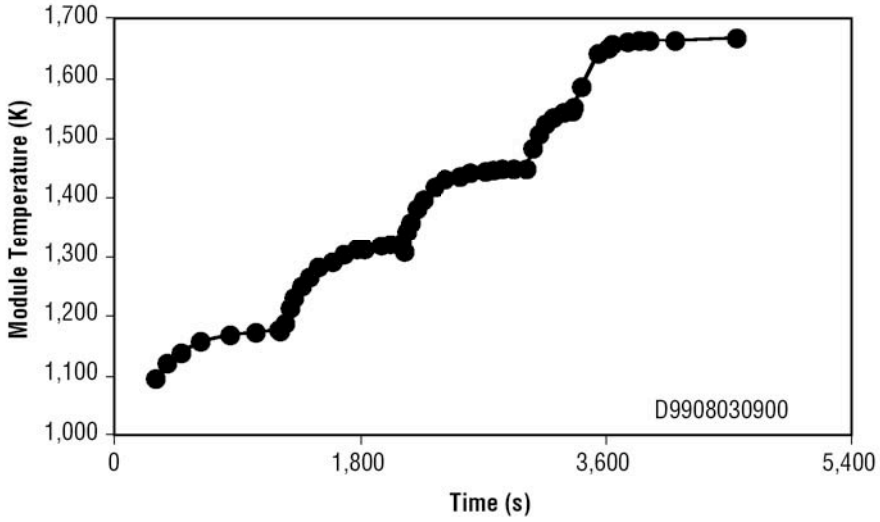

Figure 4. Time versus temperature profile for first test of the uninsulated module.

Calculations verified that the heat rejected from the module by radiation was approximately equal to that delivered to the module from the heaters. A second test, carried out with identical settings and procedures as the first test, yielded the same results. These two tests verified that the heaters could be used to realistically simulate heat from fission. In an effort to increase the available heater power, the power supply was rewired to increase current. The third test showed that at the same power levels, the time-temperature profiles were identical to the first two tests. The maximum power delivered by the heaters for the third test was ≈9.2 kW, corresponding to a maximum module temperature of 1,754 K. This temperature is higher than that required for a potential first fission propulsion flight demonstrator. These tests provided time versus temperature profiles that served as a baseline for determining performance capability of the heat pipe and demonstrated high-temperature test capability.

The next set of tests examined the operability of a heat pipe under various startup transients (slow and fast), even when exposed to extreme conditions. Type C thermocouples were installed on both the heat pipe and on the module to record temperatures. The thermocouple on the module served to (1) verify the optical pyrometer readings from earlier tests and (2) provide a frame of reference for the heat pipe thermocouples. In the slow startup, the heat pipe was brought to a maximum operating temperature of 946 °C after 115 min. Figure 3 shows the thermocouple instrumented heat pipe during test. The fast startup test brought the heat pipe to an isothermal temperature of 1,174 °C in 55 min, corresponding to a heat transfer rate of at least 3 kW.

The purpose of the first heat pipe test was to verify general heat pipe operation, instrumentation hookup, and test procedures. This test ran for a total of 115 min and demonstrated successful operation of the heat pipe. Since a slow startup of the heat pipe was desired, the power supply was initially set to deliver 60 V (0.12 W) and increased at ≈10-V increments every 10 min. This brought the heat pipe to a maximum operating temperature of 1,220 K after 115 min. Figure 5 illustrates the thermocouple data over the period of the test.

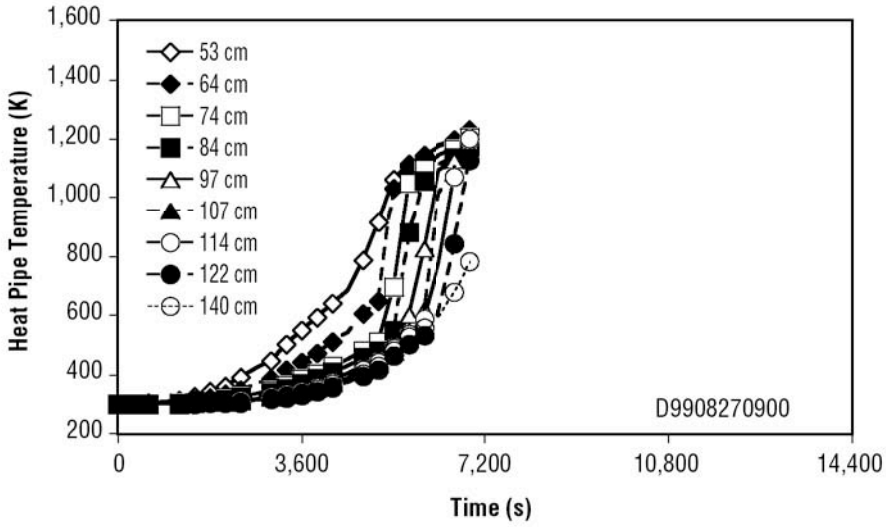

Figure 5. Startup time versus temperature profile for the first heat pipe test.

At the conclusion of the first test, air leaked into the chamber though a defective sight glass, reaching a pressure of 1 torr. To limit oxidation of the refractory metal test article, the chamber was quickly flooded with GHe to 1 atm (pumps were turned off) as the module and heat pipe cooled to ambient conditions. The module was cleaned in a hydrogen furnace followed by a second heat pipe test to determine the operational capability and verify that no damage had occurred. Since a slow startup of the heat pipe was desired, the power supply was set to deliver 60 V (0.15 W) and increased ≈15 V every 10 min. This brought the heat pipe to a maximum operating temperature of 1,395 K after 245 min. Figure 6 illustrates the thermocouple data recorded during the test period. The data indicate successful heat pipe operation with the entire heat pipe at an operating temperature greater than that of the first test (>1,220 K). At the end of the 245 min, the heat pipe was isothermal and the test terminated. The 140-cm

location (lowest temperature data) is adjacent to the liquid Li condenser pool that is built into the heat pipe. This demonstrated that the heat pipe was able to operate successfully, even when exposed to worst-case conditions. Both an optical pyrometer and a thermocouple were used for measuring the temperature of the thermocouple on the heat pipe that was closest to the module. The difference between these methods varied by a maximum of 1.5 percent, verifying the accuracy of the data recorded from the first three tests, which only made use of the optical pyrometer.

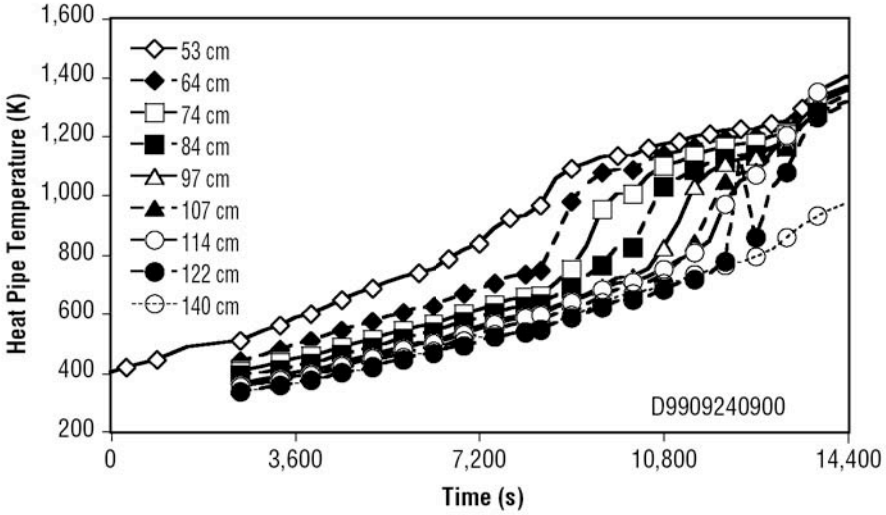

Figure 6. Startup time versus temperature profile for the second heat pipe test.

The final set of tests examined the ability of injected gas to transfer heat from the module. These tests demonstrated that gas could extract heat from the W module (producing direct thermal thrust) while withstanding the induced thermal stresses. Although the gas did not reach the desired 900 °C, the gas exit and module temperatures were identical during gas flow, indicating that the gas did extract heat from the module, tracking the module temperature as predicted.

The MUTT successfully demonstrated the use of resistance heaters to realistically simulate heat from fission. The MUTT demonstrated the ability to use several different instrumentation techniques for measuring temperature and pressure in a simulated fission (thermal hydraulic) environment. Finally, the MUTT demonstrated the energy transfer capability and operation of a heat pipe under worst-case operating conditions (fast startup and exposure to air).

1.5 Objectives of the Safe, Affordable 30-kW Fission Engine Program

The SAFE–30 test series was a full-core test capable of producing 30 kW using resistance heating to simulate the heat of fission. The 30-kW core consisted of 48 stainless steel tubes and 12 stainless steel/Na heat pipes (2.54-cm-diameter and 119-cm-length) welded together longitudinally to formulate a core similar to that of a fission flight system. As in an actual fissioning system, heat was removed from the core via the 12 heat pipes, closely simulating the operation of an actual system. LANL performed extensive neutronic analyses using the Monte Carlo neutral particle (MCNP) transport code.

The SAFE–30 and SAFE–30 end-to-end demonstrator test programs provided experimental data to anchor computational models, which predicted the temperature and heat transfer within the core,

along the heat pipes and into the energy conversion cycle. It was also used to explore the operational constraints for such a system. These data were used as a research tool supporting the development of a larger; e.g. 100-kW, core design. Funding for this testing effort was from an MSFC Center Director's Discretionary Fund (CDDF), whereas the core and heat pipe hardware valued at $250,000 was donated by LANL.

Specific objectives of the SAFE–30 tests included the following:

- Simulation of nuclear core environment (thermally) through nonnuclear resistance heaters.
- Demonstrate capability for using nonnuclear testing to develop space fission system components, evaluate full space fission system cores, and demonstrate performance of a potential phase 1 fission system core.
- Demonstrate ability of the core to efficiently transfer heat from the fuel elements to a point external to the core via heat pipes.
- Assessment of system performance and robustness of a core with heat pipes.
- Startup of the heat pipes under rapid heating conditions (from room temperature to 973 K in <1 hr).
  - Demonstration of the ability to successfully undergo multiple startups and shutdowns.
  - Demonstration of system performance with simulated heat pipe failure.
  - Heat transfer characteristics and efficiency of the heat pipes (temperature and power).
  - Determine performance of core heat pipe system operating in Mars-type environment.
- Verification of theoretical thermal analysis regarding the performance of the core.
- Assess system performance in an end-to-end demonstration where thermal energy is transferred to an energy conversion cycle.

Upon completion of the CDDF tests, the SAFE–30 was reconfigured to accomplish an end-to-end demonstration test of an NEP system. This was the first time within the United States that a hardware ground-based system of an entire concept—core, energy conversion, and an electric propulsion engine—was demonstrated. Funding for this reconfiguration was received from the MSFC In-Space Program office. Figure 7 is a pictorial representation of the core and Stirling engine. Since the purpose of this test was to show proof of concept with inexpensive off-the-shelf materials, the system was not optimized for performance; rather, the test was designed to demonstrate proof of concept and identification/resolution of integration issues for future systems.

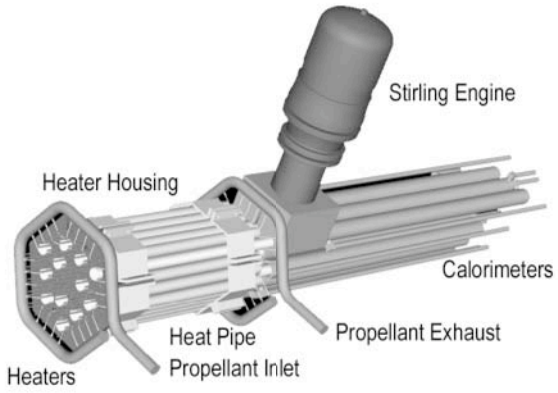

Figure 7. SAFE hardware layout (core and heat pipes).

2. TEST ARTICLE DESIGN

2.1 Heat Pipe Power System Core Designs

The SAFE–30 is one of several heat pipe power system (HPS) cores under study by LANL that can provide surface power for space missions. A wide variety of core layouts have been evaluated that use 12 to >100 modules. A schematic of a 12-module HPS (also referred to as the SAFE–30) is shown in figure 8. The fuel pins are bonded structurally and thermally to a central heat pipe, which transfers heat to an excore power conversion system. The heat pipe also provides structural support for the fuel pins. The rated power of an HPS is based on a worst-case heat pipe failure, and in most cases, multiple heat pipes can fail before a significant power decrease occurs.

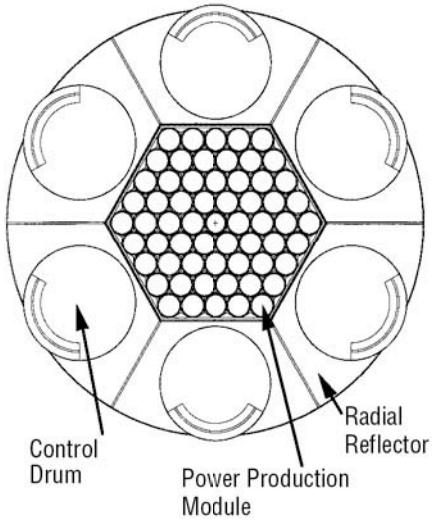

Figure 8. Twelve-module HPS.

Two fuel types have been evaluated for use in the Martian surface HPS, which include uranium nitride (UN) and uranium dioxide (UO_2). The use of UN results in the most compact, high-power core. Uranium nitride fuel pins may need to be sealed hermetically, although the peak fuel temperature will be ≈1,150 K during nominal operation and ≈1,300 K adjacent to a failed heat pipe. At these relatively low temperatures, the pins may not need to be sealed. UO_2 has a lower uranium loading than UN; however, the pins do not have to be sealed hermetically and can be operated at a higher temperature than UN pins, although this is not an issue for a nonrefractory core, which is clad temperature limited. One advantage of UO_2 is that there is a larger experience base and production capability for this fuel. For both fuels, burnup limits (based on experimental results) are not reached for several decades in most designs. Carbide and advanced fuels could also be considered for the Martian surface HPS.

Several options are available for cladding the Martian HPS. Some of the most promising candidates are stainless steel, Special Metals Corporation's Inconel®, and HT–9. Several other superalloys could be considered, and there is even the potential that a refractory metal could be used if tests show little corrosion or if a robust coating is developed. Simple corrosion testing in a simulated Martian atmosphere could help narrow down the field of candidate materials. For the purposes of this study, two materials were considered—stainless steel and Inconel. The Martian HPS cores are designed so that the clad temperature does not exceed 1,050 K for a worst-case heat pipe failure. (The maximum clad temperature is closer to 950 K during nominal operation.)

The nonrefractory HPS core will run at relatively low temperatures (<1,000 K); therefore, Na or potassium (K) are best suited for the heat pipe working fluid. There is more experience with Na- and K-based heat pipes than any other type of high-temperature liquid metal pipe. There is also considerable irradiation data on these types of heat pipes. A total of 29 liquid metal heat pipes have been irradiated to significant fast neutron fluences, with no failures. A stainless steel/Na heat pipe operated at 1,100 K to a fast fluence of 2.2×10^{22} n/cm^2, which is more than an order of magnitude higher than that required by most potential near-term HPS missions.

Neutronic and thermal calculations have been performed to optimize the mass and power level of various HPS core geometries. Criticality and power density calculations were performed with MCNP transport code. Each core is designed with a cold, clean k-effective of 1.03. These cores will need to contain additional neutron-absorbing material in the interstitials at launch, or will have to be launched partially fueled. (Total passive safety may be achieved with a mass penalty of ≈50 kg.) Thermal calculations were performed with a three-dimensional finite-difference FORTRAN code. This code discretely models each pin (fuel, gap, and clad), the heat pipes, and the shroud. The most significant limitation of the model is that the heat pipes are simply modeled with a constant temperature boundary condition on the inner wall, which should be reasonable for steady-state calculations. The thermal power is based on a maximum clad temperature of 950 K, and a heat pipe temperature of 923 K. The calculations assume a surface emissivity of 0.4, which is probably conservative because the stainless steel will become carbonized, and the presence of the Martian atmosphere in all gaps (≈5 mbar carbon dioxide (CO_2)). It is also assumed that each pin and heat pipe are brazed to an interstitial stainless steel tricusp on all sides, as is being done for the HPS full-core demo, discussed in this section.

UO_2 and UN designs were evaluated for each of the geometries considered. Due to the higher uranium (U) loading and higher thermal conductivity of UN, the UN cores on average produced much higher power (38 percent) at a lower mass (–33 percent). The advantage of using UN instead of UO_2 in criticality-limited stainless steel or superalloy systems is much larger than the advantage seen for refractory metal systems. In stainless steel or superalloy systems, performance is limited by the maximum allowable clad temperature. In other words, when the maximum allowable clad temperature has been reached, the peak fuel temperature is still well within the temperature capability of UN fuel. The higher U density of UN fuel reduces the critical size of the core. Because of the higher performance, the nitride system is considered the baseline, although issues, such as sealing the pins if required, fabrication availability, existing nuclear data, or other issues, could favor UO_2. Inconel designs were also evaluated for each geometry. In each case, the Inconel design provided slightly lower power (–3 percent) at a slightly higher mass (2 percent). This, plus the fact that Inconel parts are more difficult to fabricate and are more expensive, led to the choice of stainless steel for the baseline designs. This is

not to say the Inconel, HT–9, or any other material might not be the best choice. There will be several factors other than neutronic and thermal performance that will drive the decision, such as corrosion in CO_2, radiation damage characteristics, and existing nuclear database. Table 2 is a summary of stainless steel-clad UN HPS cores that are not fully optimized.

The mass listed in table 2 includes the core, core support, primary heat transport, and reflector, but does not include power conversion, heat rejection, shielding, etc. The clad, heat pipes, tricusps, and structure are SS–316. The fuel is 97.6-percent enriched UN at 13.56 g/cc (96-percent TD); matching the specification of existing SP–100 fuel at LANL TA–55. The reflector is beryllium oxide (BeO) and is clad with 1-mm stainless steel. The core shroud is 2-mm stainless steel and the upper and lower support plates are 1-cm stainless steel. The poison on the control drums consists of a 1-mm layer of molybdenum-rhenium (Mo-Re) sandwiched between two 5-mm layers of boron carbide. (The use of sliding reflector would lower mass slightly.) The axial reflector region contains BeO pellets within the fuel pins. The highest power cores require very high-performance heat pipes, and may require some additional development. (The heat pipe requirements could be relaxed with a slight mass penalty.)

Table 2. Summary of stainless steel clad, UN-fueled HPS cores.

Design Parameter	HPSMARS1	HPSMARS2	HPSMARS3	HPSMARS4	HPSMARS5
Number of heat pipes	12	19	30	57	121
Number of fuel pins	48	102	138	152	336
Core flat-flat dimension (cm)	20.2	18.2	18.4	20	21.8
Core active length (cm)	34	31	34	37	36
Axial reflector length (cm)	4	4	4	4	4
Pin length (cm)	42	39	42	45	44
Reflector thickness (cm)	6.5	6.2	6.4	6.5	6
Reflector outer radius (cm)	17.1	15.8	16.1	17	17.4
Reflector height (cm)	38	35	38	40	40
Control drum radius (cm)	3.25	3.1	3.2	3.25	3
Pin outer diameter (cm)	2.54	1.6	1.4	1.35	1
Clad thickness (mm)	1.27	0.51	0.51	0.51	0.51
Reactor power (kW)	**40**	**50**	**85**	**350**	**640**
Nominal operation					
Power to heat pipes (kW)	38.2	48.8	83.1	347.6	637.4
Maximum fuel temperature (K)	1,077	1,150	1,069	1,191	1,198
Maximum clad temperature (K)	1,074	1,113	1,064	1,172	1,170
Maximum heat pipe power (kW)	3.6	3	3	7.2	6
Maximum radial heat flux (W/cm^2)	17.4	21.3	25.6	59.2	68.4
Maximum axial heat flux (kW/cm^2)	0.8	1.8	2.4	6.3	9.4
Worst case failed heat pipe					
Power to heat pipes (kW)	**37.7**	**47.8**	**82.8**	**347.6**	**637.4**
Maximum fuel temperature (K)	1,270	1,286	1,264	1,260	1,262
Maximum clad temperature (K)	1,253	1,246	1,249	1,248	1,244
Maximum heat pipe power (kW)	4.8	3.4	4.2	8.6	7.2
Maximum radial heat flux (W/cm^2)	26.7	26.9	41.6	81.2	93
Maximum axial heat flux (kW/cm^2)	1.1	2.1	3.3	7.5	11.2
Mass (kg)	**195**	**153**	**173**	**199**	**217**
UN mass (kg)	90	75	83	92	101
Cold, clean k-effective	1.031	1.034	1.032	1.029	1.030
Fuel burnup per year (%)	0.019	0.029	0.044	0.164	0.272

The power capability of the HPS is highly dependent on the temperature delivered to the power conversion system. Maximum power is determined by the maximum allowable temperature difference between the fuel and heat pipe. To be conservative, it is also assumed that the worst-case heat pipe failure has occurred, thus maximizing the temperature difference. If the system is designed for a 273 K temperature difference (maximum fuel to heat pipe ΔT), then power output could be doubled by operating the heat pipes at, for example, 700 K instead of 973 K, provided the heat pipes were designed to carry the additional power at 700 K. The lower heat pipe temperature would allow twice the conductive temperature difference between fuel and the heat pipe, providing approximately twice the power density (small differences due to variable thermodynamic properties and radiation nonlinearity). If significantly different power levels are desired (more than a factor of 2 or 3), then it is probably best to redesign the entire system for the different power level.

The 12-module design (HPSMARS1) was the unit manufactured for the SAFE–30 full-core demo. This design specifies a thicker clad because it is the standard dimensions of the tubes chosen for the demo. The other designs specify a rather thin clad because of the relatively low burnup. (The lower power cores would take several decades to reach 1-percent burnup.) If necessary, the clad can be made thicker for a small mass penalty. In table 2, the higher power cores have a larger heat pipe-to-fuel pin ratio and smaller diameter pins. The large heat pipe-to-fuel ratio also results in a slight mass increase; for example, with a 42-percent increase in mass comparing cases 2 and 5, there is a 1,250-percent increase in power. At very high powers (>3,000 kW thermal power), it may be desirable to design modules that consist of cylindrical fuel pins surrounded by noncylindrical heat pipes. Limited data are available on noncylindrical heat pipes, but such data can be obtained inexpensively by testing electrically heated modules. Another high-power approach would be to utilize a "monolithic" core.

Advanced Methods and Materials of San Jose, CA, has developed a brazing technique for the HPS module that provides excellent mechanical and thermal bonding. In all tests to date, diagnostics, including acoustic microscopy, have verified that a robust braze has been achieved. Future systems may utilize brazed modules, or could use alternative manufacturing techniques; e.g., hot isostatic pressing (HIP).

2.2 Safe, Affordable 30-kW Fission Engine Core Description

The SAFE program will perform realistic system level testing of a fission-based first-generation propellant energy source. Heat from fission will be closely simulated using resistance heaters. The core that will be tested was designed and fabricated by LANL, and if fueled and reflected, would operate as a nuclear system. Testing of the core will provide information valuable to the design and development of a first-generation propellant energy source and build confidence that such a system is feasible. This will also demonstrate that significant progress in space fission system development can be made via nonnuclear testing at ordinary facilities.

The SAFE–30 test article consisted of 48 stainless steel tubes and 12 stainless steel/Na-filled heat pipes brazed and banded together to form a core similar to that of a fission flight system (fig. 9). Electrical resistance-type heaters are inserted into the 48 tubes to simulate heat from fission. (UO_2 or UN would fill the tubes if heat was being generated by fission.) LANL performed analyses verifying the core would operate as a fission system if U fuel and a neutron reflector were added. This analysis

has been confirmed by Sandia National Laboratories, the Russian Institute for Physics and Power Engineering (responsible for all 33 Soviet fission system launches), and Russia's Kurchatov Institute. The core consists of 12 modules (figs. 9–11). Each module consists of a heat pipe (heat is removed from the core via the heat pipes) and four adjacent tubes brazed together longitudinally, utilizing a tricusp to fill the interstitials between the tubes. The heat pipes were designed, fabricated, and tested at LANL before being sent to MSFC. The stainless steel heat pipes have a 1-in diameter, 51.2-in length, and have a sealed tube design filled with Na. Within the heat pipe is a composite annular wick structure consisting of a 100-mesh inner support layer, 400-mesh middle capillary layer, and 60-mesh outer liquid phase layer. The meshes provide the means of transferring the liquid Na from the condensing end to the evaporator end. Although each heat pipe is only required to carry 2.5 kW (heat removal limitation of the facility at this time), each heat pipe was designed to transport up to 20 kW. Dimensions for the four 304 stainless steel tubes brazed to the heat pipe were a diameter of 1 in, a length of 17 in, and a wall thickness of 0.065 in. An electrical resistance-type heater cartridge is slid into each of these tubes to provide the simulated fission heat. The modules were bundled together by three stainless steel bands. Each band was made up of six bent segments, ≈3 in wide by 0.25 in thick, loosely bolted to allow for thermal expansion of the core. The outer two bands rest on a 0.75-in-diameter alumina tube extending beyond the heated portion of the core and providing support (connecting to four support legs).

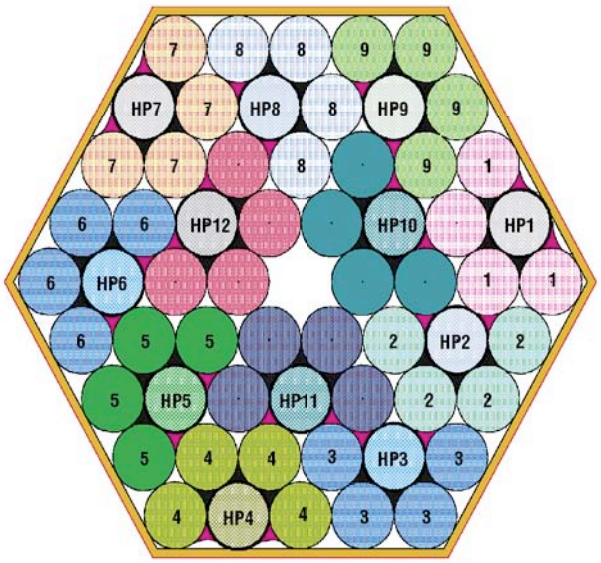

Figure 9. Cross section of core assembly—12 modules are assembled to make entire core.

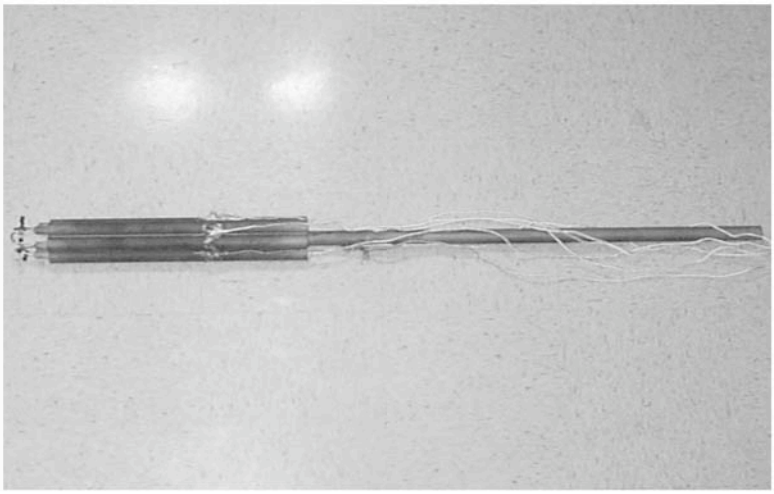

Figure 10. SAFE–30 module.

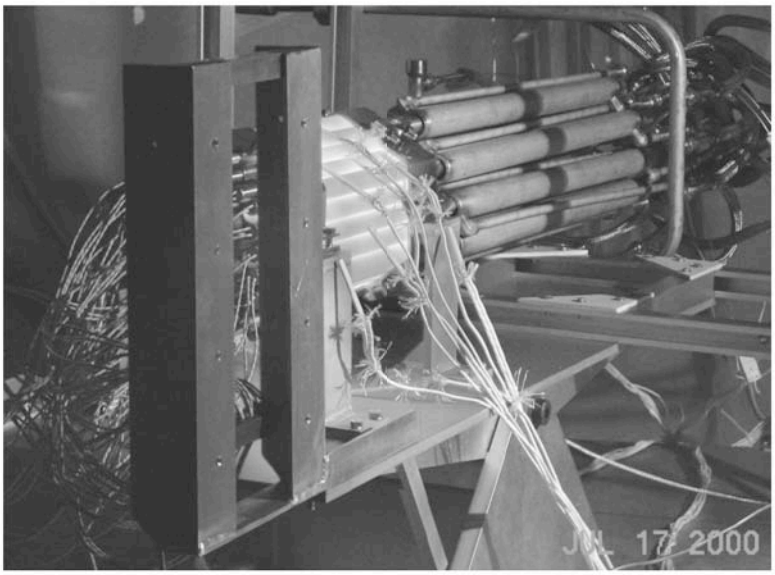

Figure 11. SAFE–30 being tested at MSFC.

2.3 Heat Pipe Module Design, Fabrication, and Testing

2.3.1 Heat Pipe Module Construction

A cutaway drawing of a heat pipe module with four cartridge heaters inserted into the module fuel tubes is shown in figure 12. Heat pipe dimensions are given in table 3. The heat pipe envelope consisted of a 304 stainless steel seamless tube having a 2.54-cm OD and a 1.65-mm-thick wall. The end caps were identical in composition. A crescent annular wick was chosen to simplify construction, ensure robustness, and to minimize axial pressure drop in the liquid region. The wick was fabricated from 304 L stainless steel screens that had been chemically cleaned and vacuum fired at 1,025 K for several hours. The annular wick consists of one support layer of 100-mesh screen on the inside diameter (ID), three capillary pumping layers of 400-mesh screen, and two outer liquid flow layers of 60-mesh screen. The screen layers were wrapped around a Cu rod drawn to 1.73-cm OD and were retained by wire-to-wire spot welds at ≈2-mm intervals on the outside layer of screen. After wrapping, the Cu rod was slid out of the wick assembly. The evaporator end of the wick tube was sealed to the 400-mesh screen layers with a fitted stainless steel plug and mechanically retained with an Ni wire wrap. The annular wick was checked for capillary pumping capacity in an ethyl alcohol bath using He as a pressurizing gas. Tests confirmed that the maximum pore radius was <47 μm. Final wick dimensions were 1.74-cm ID and 2.07-cm OD. The 0.17-cm-thick wick assembly formed a rigid tube, which, when inserted into the heat pipe container, left a 0.07-cm annular gap.

A fill stem was tungsten inert gas (TIG) welded to the condenser end cap. The wick was placed inside the stainless steel tube and the end caps were TIG welded to the tube body. Each weld was inspected and leak tested. The heat pipe interior was fired at 10^{-5} torr and 1,025 K for several hours. After firing, the heat pipe was filled with 77 kPa argon (Ar) and its fill stem sealed with a compression fitting. The heat pipe was delivered to a commercial vendor where four 43-cm-long, 2.54-cm-OD fuel tubes were brazed to the evaporator end of the heat pipe, forming the module assembly. The braze was made at 10^{-5} torr and 1,325 K over an 8-min period. After braze, the module was returned to LANL. The inside of the module was vacuum fired for several hours at 10^{-6} torr and 1,073 K.

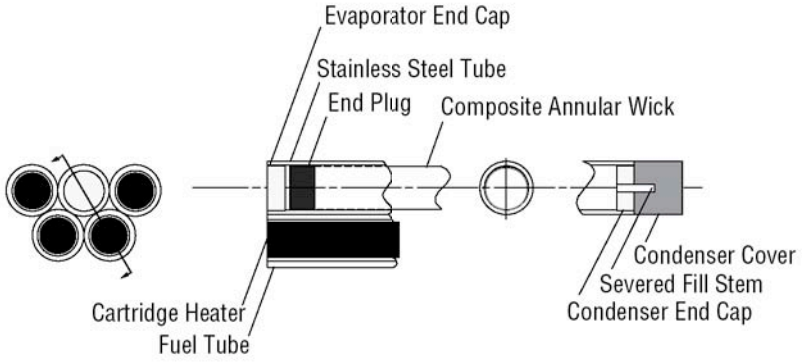

Figure 12. Cutaway view of stainless steel/Na heat pipe module.

Table 3. Heat pipe module dimensions.

Item	Value
Heat pipe length	120 cm
Evaporator length	43 cm
Condenser length	77 cm
Heat pipe outside diameter	2.54 cm
Heat pipe inside diameter	2.21 cm
Wick outside diameter	2.07 cm
Annular gap thickness (on radius)	0.07 cm
Wick inside diameter	1.74 cm
Wick thickness	0.17 cm
Effective pore radius	47 μm
Module weight after distillation	3,785.6 g
Module tare weight	3,640.3 g
Sodium transferred to module	145.3 g
Wet in temperature	875 K
Wet in time	49.5 hr

The heat pipe was distillation filled with 145 g of DuPont® Niapure® Na. The charge quantity filled the wick void volume, annulus volume, and surface cavities, and left some excess for dimensional uncertainty. After fill, a Cu chill block was attached to the fill stem and the Na melted and gravity fed to form a solid plug of Na at the condenser end. The heat pipe was brought to 1,073 K over its entire length inside a furnace (with fill stem-chill block outside the furnace) open to atmosphere for 48 hr. This step allowed Na to wet the heat pipe's internal surfaces. Qualification testing consisted of bringing the module's evaporator exit to 950 K in air with four 43-cm-long, 1.9-cm-diameter cartridge heaters. Before shipment to MSFC, the Na inventory was again transferred to the condenser end of the module. The condenser end of the heat pipe was stripped of oxide. The fill stem was cut from the module body inside an Ar atmosphere, exposing solid Na. An end cover was electron beam welded to the condenser end, sealing the module.

2.3.2 Test Procedure and Results

Upon arrival at MSFC, the Na inventory that had been solidified at the condenser end of the heat pipe was melted and moved toward the evaporator end. The oxide layer that had formed on the outside module surface during test at LANL was removed by bead blasting. The module was rested horizontally on a stainless steel frame and placed inside a vacuum chamber so its evaporator and two fuel tubes could be viewed through a sight glass on the side of the chamber. Unoxidized cartridge heaters were inserted into each fuel tube, wired in parallel, and connected to a voltage-controlled ac power supply. Power to the module was found by measuring the terminal voltage and total current through a shunt. Type C thermocouples were spot welded at three locations on the fuel tubes and at five axial locations along the heat pipe length. Figure 13 shows the thermocouple placement used during this test.

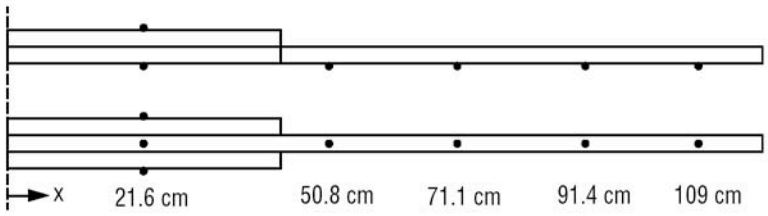

Figure 13. Thermocouple placement on fuel tubes and heat pipe during test.

The error limits for type C thermocouples cited by the manufacturer are 4.5 °C at 698 K. This error limit is in addition to any uncertainty introduced by imperfect thermocouple attachment to the module surface and local heat loss from the module surface through thermocouple wires. The chamber was brought to 10^{-5} torr pressure. Power was increased to the module in 80-W increments at 5-min intervals. The electrical curve in figure 14 shows the measured electrical power to the module versus time. At 3 hr into the startup ramp, power to the module was 2,600 W. Power was held at this level for 30 min. The module was cooled by reducing power in 160-W increments at 5-min intervals. The total hemispherical emittance of bead-blasted module surfaces was estimated to be 0.4 (from values found in the literature and from consistency in temperature and power data taken during test). Assuming heat transfer between long concentric cylinders, the power balance around the cartridge heaters is:

$$q_{\text{electrical}} = m_{CH} c_{p,CH} \frac{dT_{CH}}{dt} + \frac{\sigma A_{CH}\left(T_{CH}^4 - T_{FT}^4\right)}{1/\varepsilon_{CH} + A_{CH}/A_{FT}\left(1/\varepsilon_{FT} - 1\right)} \quad . \tag{1}$$

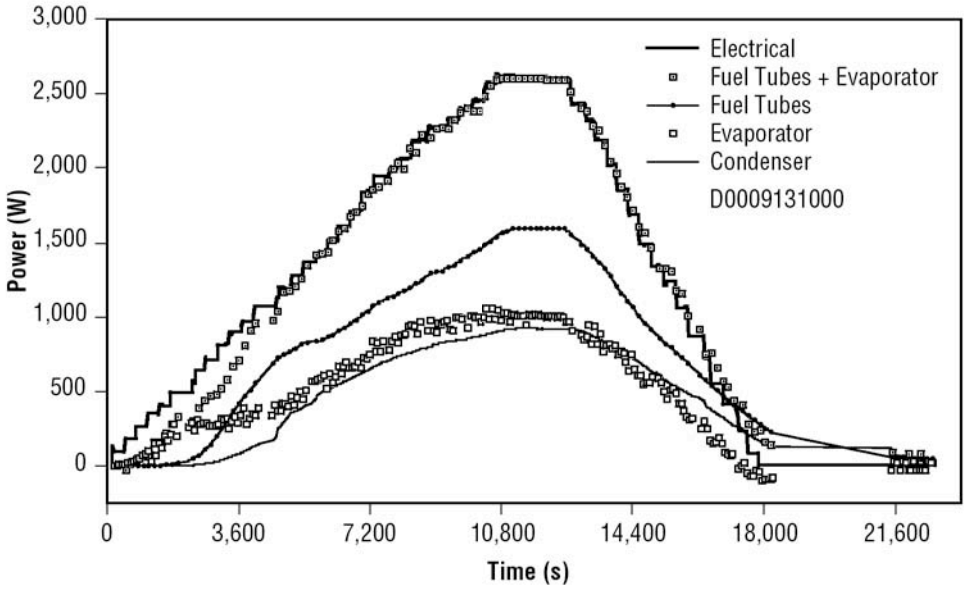

Figure 14. Various heat transfer rates around the module versus time.

Since $q_{\text{electrical}}$ and T_{FT} are measured, T_{CH} can be solved in equation (1) at each time step giving the radiation heat transfer rate between the cartridge heaters and the fuel tubes. A power balance around the fuel tubes includes the heat transfer rate from the fuel tubes to the evaporator, the radiation exchange between the cartridge heaters and the fuel tubes, the heat capacity of the fuel tubes, and the radiation exchange between the fuel tubes and the surroundings:

$$q_{\text{evaporator}} = \frac{\sigma A_{CH}\left(T_{CH}^4 - T_{FT}^4\right)}{1/\varepsilon_{CH} + A_{CH}/A_{FT}\left(1/\varepsilon_{FT} - 1\right)} - m_{FT}c_{p,FT}\frac{dT_{FT}}{dt} - \varepsilon_{FT}\sigma A_{FT}\left(T_{FT}^4 - T_{\infty}^4\right) . \qquad (2)$$

The fuel tubes plus evaporator data points in figure 14 give the radiation heat transfer rate between the fuel tubes and surrounding chamber and the heat transfer rate to the evaporator. Early in startup, cartridge heaters and fuel tubes absorb sensible heat and the electrical curve leads the fuel tubes plus evaporator data points. During module cooling, the curve also leads the data points on the downward slope. The fuel tubes curve in figure 14 gives the radiation heat transfer rate from fuel tubes to the surroundings chamber. At the peak operating power, the total radiation heat transfer rate from fuel tubes to the surroundings was ≈1,600 W.

The evaporator data points in figure 14 give the heat transfer rate from the fuel tubes to the heat pipe evaporator. The electrical curve is the total electrical power dissipated by the cartridge heaters. The fuel tubes plus evaporator curve is the radiation heat transfer rate from surface of cartridge heaters. The fuel tubes curve is the radiation heat transfer rate from the fuel tubes to the surroundings. The evaporator curve is the heat transfer rate defined by equation (2). The condenser curve is the heat rejection rate defined by equation (3) and includes the radiation from the unheated side of the evaporator.

Near the maximum operating power, resistance across the brazed joint made the heat pipe surface ≈75 K cooler than the fuel tubes. Thermal power was rejected from the heat pipe condenser by radiant exchange with water-cooled vacuum chamber surfaces. Condenser temperature data were used to estimate the condenser heat rejection rate. The net radiant energy rate between condenser surface and its surroundings is:

$$q_{\text{condenser}} = \sigma\varepsilon p\sum_{i=1}^{N_C}\left(z_{i+1} - z_i\right)\left(\frac{T_{i+1}^4 + T_i^4 + T_{i+1}^3T_i + T_i^3T_{i+1} + T_{i+1}^2T_i^2}{5} - T_{\infty}^4\right) . \qquad (3)$$

The unity coefficient in the $T_{i+1}^2T_i^2$ term in equation (3) corrects equation (9) in "Transient Tests of a Molybdenum-Lithium Heat Pipe" (Reid et al., 1999), which has a coefficient of 2 leading the equivalent term. The total radiation heat transfer rate from the heat pipe condenser surface, including the evaporator area not covered by fuel tubes was ≈925 W at 900 K. The condenser curve in figure 14 gives a condenser heat rejection rate that includes radiation between the unheated side of the evaporator and the chamber walls. The evaporator heat rejection rate exceeds the condenser heat rejection rates at the peak power by ≈90 W. Besides measurement uncertainty, radiation heat transfer between the evaporator end cap and the surroundings and between the noninstrumented pool region and the surroundings accounts for part of this 90 W.

The wall temperature at locations along the heat pipe during the startup is shown in figure 15. The slope of the temperature versus time profile at the first thermocouple location increased from near zero at 1,800 s to 13 K/min at 3,600 s. The slope of the temperature versus time profile diminished as continuum flow was approached locally. Except for the 10-cm-long condenser pool, the heat pipe became isothermal at 850 K, 2 hr into the startup. Power was increased to the heat pipe until it reached 900 K at the evaporator exit. At this point, the heat pipe surface temperatures agreed within 5 °C along the active length of the heat pipe. The module dwelled near 900 K for 30 min. Pyrometer readings confirmed that the exposed evaporator was isothermal to within measurement accuracy. Power was then decreased to the module at twice the rate that power was applied during startup.

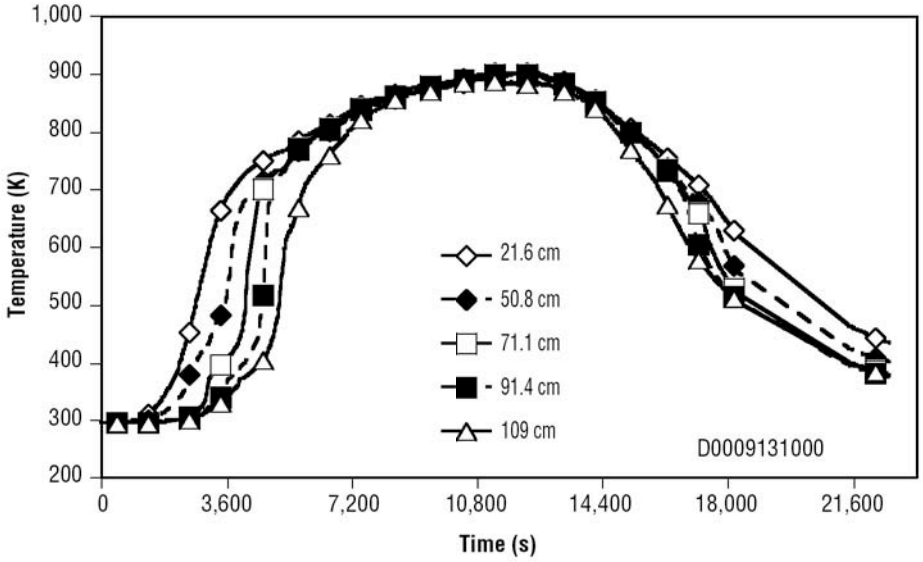

Figure 15. Heat pipe surface temperatures measured during the 7-hr test to 900 K. Distance in legend is measured from the evaporator end cap.

Figure 16 compares the condenser heat rejection rate to the steady-state sonic and viscous limits at various evaporator exit temperatures. The condenser heat rejection rate used in figure 16 omits radiation from the unheated evaporator side. The dashed curve shows the sonic heat transfer rate limit; and the solid curve shows the viscous heat transfer rate limit. The open triangles represent data taken during startup. The open inverted triangles represent measurements made during shutdown. At 650 K evaporator exit temperature, axial conduction through the stainless steel heat pipe container was the dominant heat transfer mechanism. The melt front had progressed to the condenser end, but the Na vapor pressure was still quite low. As the evaporator temperature increased, the vapor density and the axial pressure gradient in the core region became sufficient to move vapor into the heat pipe condenser. The condenser heat rejection rate followed the viscous heat transport limit up to 750 K. Above 750 K, heat transfer through the heat pipe was limited by the radiation coupling between the condenser and its surroundings. In the radiation-limited mode, there was a reduction in the slope of the heat rejection rate versus evaporator exit temperature curve. The heat pipe became fully isothermal as it approached 850 K. The condenser power curve continued in the radiation-limited mode up to a peak 764 W throughput at 900 K.

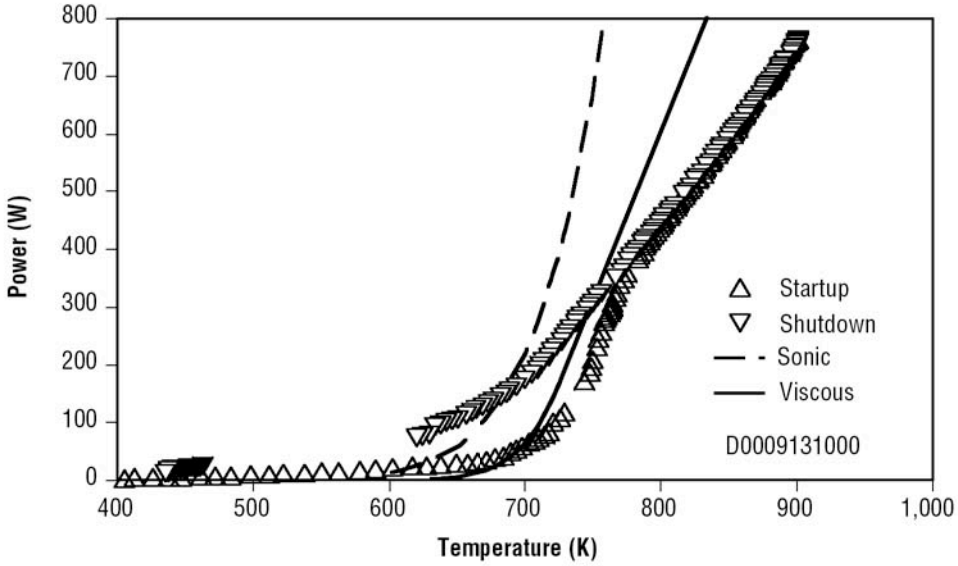

Figure 16. Condenser heat rejection rate versus temperature near the evaporator exit during module startup (Δ) and shutdown (∇).

3. TESTING

3.1 Facilities and Test Article Setup

The SAFE–30 was tested in a 12-ft-diameter by 12-ft-long horizontal vacuum chamber located in building 4776 at MSFC. The chamber is of stainless steel construction and equipped with a roughing train consisting of six 32-in-diameter Varian diffusion pumps and three Stokes 1722 packages. The chamber head rests on rails and may be rolled back to provide access into the chamber. The test article was viewed through two sight glasses and illuminated by a quartz lamp located inside the chamber. Chamber cooling was not required, since it was too massive to heat significantly during any typical test. A ventilation exhaust fan and duct were connected to the chamber to help remove any noxious fumes following a test.

Significant effort was place on using off-the-shelf, reasonably priced heaters. However, heater failures due to trapped gases inside the heater during fabrication caused premature shutdown during the first two test runs so an alternative was needed. Fortunately, a design and fabrication program focused on developing high-temperature/high-power heaters was already in progress within the Propulsion Research Center (PRC) to support the planned SAFE–300 testing. It was decided that these PRC "home built" heaters would be used as replacements for the commercial units and testing continued. This new heater design had already been bench tested, meeting the requirements of both the SAFE–300 and SAFE–30 test programs.

The element portion of these heaters was made of graphite manufactured by Poco Graphite, Inc. The electrical leads consist of 4-in-long, 0.06-in-diameter Mo wire inserted into a stepped hole (0.094-in diameter by 0.5-in deep, stepping down to 0.059-in diameter by 0.5-in deep), and cemented into the graphite using graphite cement cured for 4 hr at 130 °C. Alumina sleaving was slid over and cemented to the graphite-heated element to provide both a means of centering the heater and electrically insulating the heated element from the stainless steel tubes of the core as shown in figure 17.

Figure 17. MSFC-fabricated graphite heaters.

Because two modules were damaged during shipping to MSFC, the SAFE–30 was assembled with an initial configuration of nine working modules and three "dummy modules" (internal three modules of the core). Since there were four pins (heaters) per module, the heaters were wired in two parallel sets of two heaters in series. Ten power controllers were wired to the heaters to control each module—a separate controller for each of the nine outer modules that have working heat pipes, and a single controller for the three modules that had dummy heat pipes. The wires connecting the heaters' leads were solid 12-gauge Cu, covered with Siltemp® sleaving as they were routed to terminal strips.

Junctions to the heaters' leads were made with brass screw-down clamping lugs. Standard, 105 C-rated insulated wire was used from the Jones strips to the chamber feedthroughs. Standard Varian Corporation ConFlat® mounted power feedthroughs were used with 30-A capacity for each control zone. The power controllers were supplied by individual breakers on a 480-V, three-phase service panel. An NI SCXI data acquisition and control (DAQ) chassis model 1001, connected to a PCI–MIO–16E4 DAQ card in a personal computer, was used for DAQ of the power controllers. An NI analog input/output board, model SCXI–1124, was used to send a 4- to 20-mA command signal to each of the power controllers. Multiple thermocouple (TC) dc voltage input boards, model SCXI–1102, were used to acquire the TC, voltage, current, flowmeter, vacuum transducer, and flow switch signals. The voltage and current delivered to the chamber penetration for each power controller was measured using transducers manufactured by Flexcore®. Chamber vacuum pressure was measured using 1,000-torr and 1-torr range capacitance manometers and two nude ion gauges. Calorimeter coolant flow was measured via calibration (time required to flow 100 cm^3 of water). Type K thermocouples were used to measure temperatures. Each of the 12 modules of the core was instrumented with six thermocouples. High-temperature 3M™ Nextel™ insulated thermocouple wire was beaded and spot welded to the heat pipes and stainless steel tubes that house the heaters. The TC wires were routed to a junction panel inside the chamber. Since the chamber's instrumentation feedthrough port had a low view factor to the heated test article, DuPont® Teflon®-insulated TC wire was used from the junction panel, out through the chamber's penetration, and on to the NI chassis. The test article support structure and chamber wall also had thermocouples attached to provide information for the thermal modeling.

The NI hardware was controlled using LabVIEW. The LabVIEW virtual instument was written to record the data to a text file, control the heater's power controllers, provide alarms to notify the operator, and provide automatic safeguards to help prevent overheating of the experiment. The software displayed the data on graphic representations of the hardware and provided real-time graphs to better visualize the test progression. The software was designed to give visual indication of excessive temperatures using color and flashing displays. It commands a power controller to zero if an excessive current is measured to help prevent shutdown due to tripped breakers and blown fuses.

Calorimeters had been designed and fabricated to slide over the heat pipe condenser end to increase the amount of heat transferred down the heat pipe (fig. 11). The calorimeter consisted of a double-walled stainless steel tube, providing a jacket to contain cooling water. The inside surface of the calorimeter (exposed to the heat pipe) had been coated with a flat, black enamel, providing a high emissivity. Two alumina rings, each 1 in long, were slid over each heat pipe to provide a means of centering the calorimeters over the heat pipe as there was 3/16 in of diametrical clearance between the OD of the heat pipe and the ID of the calorimeter. The supply water was distributed to each calorimeter using a manifold. The cooling water outlet temperature was measured for each calorimeter.

3.2 Testing the Core Design

The four initial tests validated operation of the test apparatus and heat pipes. Due to unforeseen transportation difficulties resulting in damaged modules, only 10 out of 12 modules had operational heat pipes. Two replacement modules were fabricated; however, a hollow steel tube was brazed in place of the heat pipe. Initial test results show that the core achieved an operating temperature of

≈600 °C with operating heat pipe temperatures of 550 °C. Due to the difficulty of maintaining a constant high temperature with the original power supply/voltage controller configuration, tests 5 through 7 incorporated the newly developed in-house heater design and a large Variac® power controller. The result was three operational control zones, balanced to limit the power delivered to the simulated heat pipe modules while maintaining the full performance of the 10 working modules. Additionally, calorimeters were incorporated to measure heat transfer. The three heat pipes positioned nearest the core center achieved a temperature of 723 °C prior to heaters reaching a maximum voltage/current condition. Figure 18 illustrates the temperature profile for these three internal heat pipes. Thermocouples on the evaporator section of the heat pipe are called out as HP No. 10 – TC No. 1 through HP No. 12 – TC No. 2. HP No. 10 calorimeter through HP No. 12 calorimeter refers to the thermocouples at the evaporator exit. Condenser temperatures were not measured since calorimeters were in place.

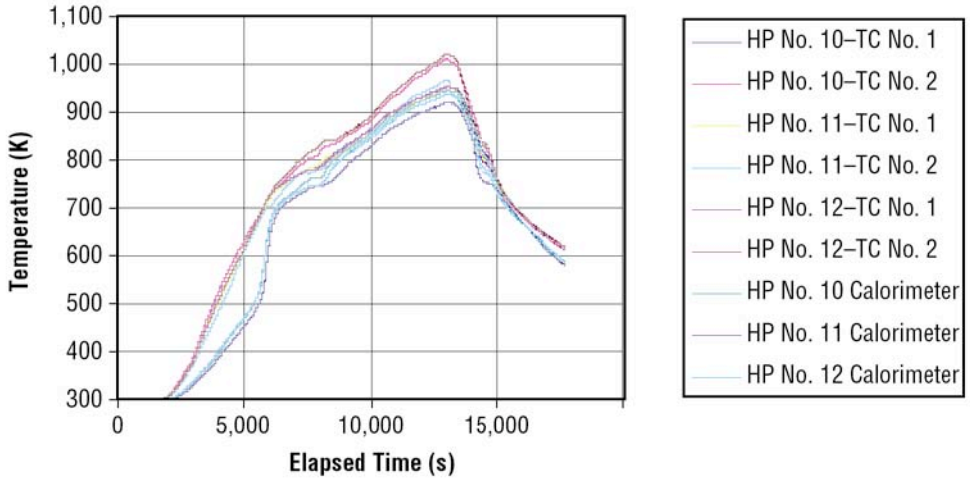

Figure 18. Operational SAFE–30 heat pipe temperatures.

Thermocouples were placed at each calorimeter exit to measure the temperature rise of the cooling water. Flow rates were measured at the beginning of the tests and verified at the end of the tests. For test 7, ≈10.7 kW were removed via the calorimeters. Additional heat could have been removed if the coupling between the heat pipes and calorimeters was improved. The low-pressure CO_2 atmosphere tests improved the coupling significantly, increasing the extracted power as measured by the calorimeters. Figures 19 and 20 show the core setup and operation within the vacuum chamber.

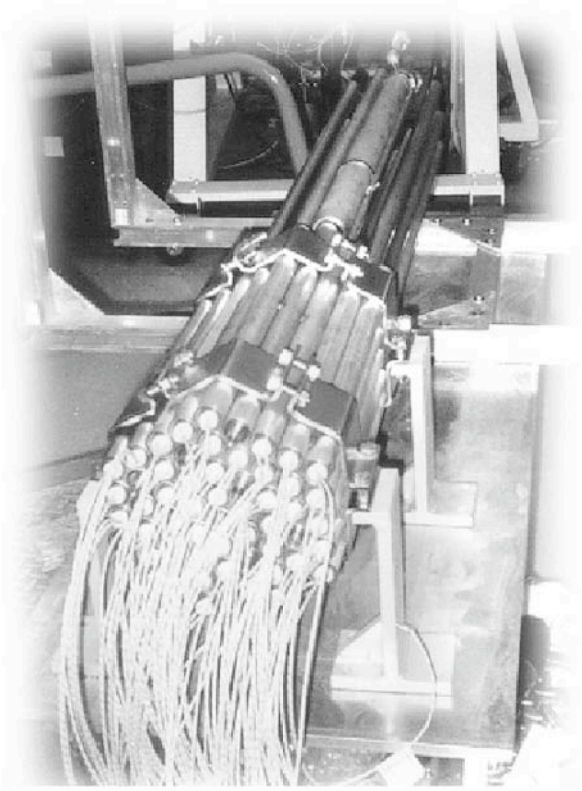

Figure 19. SAFE–30 core with resistance heaters, heat pipes, and calorimeters.

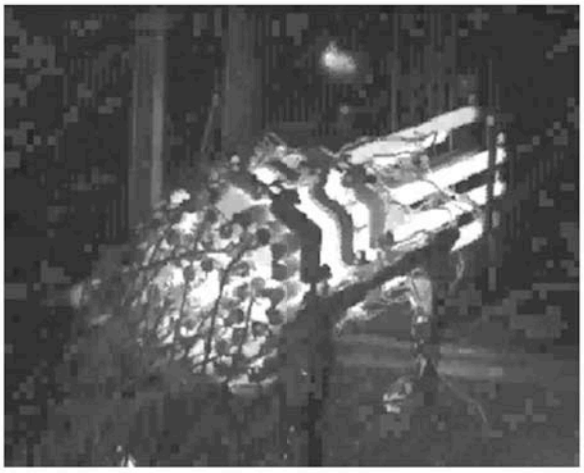

Figure 20. Operational SAFE–30 core with heat pipes at ≈600 ºC.

3.3 Posttest Analysis

A total of 84 thermocouples were positioned on the core and heat pipes, providing temperature data critical to characterizing the overall heat transfer. Additional thermocouples were added as the test program evolved. Figure 21 indicates the location of the 60 thermocouples placed within the core. The remaining thermocouples were divided: 12 placed on heat pipes (one per pipe) just outside the core used to represent the heat pipe temperature and 12 placed on calorimeter exits.

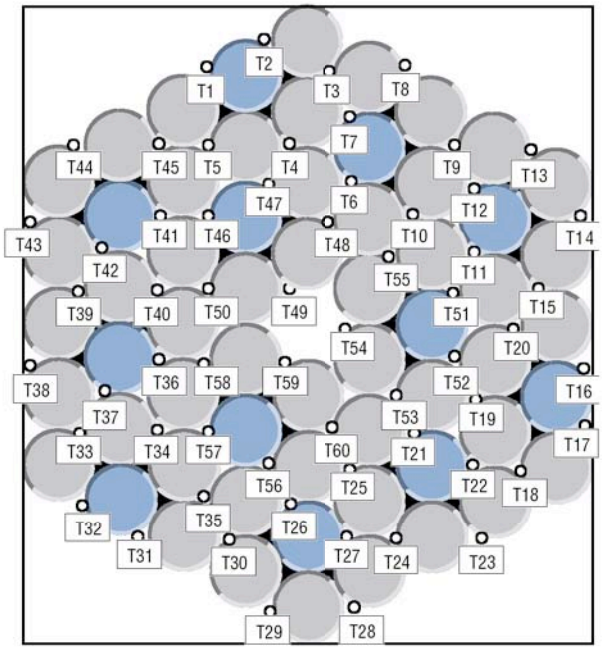

Figure 21. Placement of thermocouples in the SAFE–30 core.

Vacuum chamber pressure was monitored with an MKS Instruments 1,000-torr Baratron®, 1-torr Baratron, and two ion gauges, providing full coverage from atmospheric pressure to hard vacuum. A 0.75-in flowmeter was used to record the total flow through either the heat pipe calorimeters or the Stirling engine, selected by the test. There were also 12 independent controllers used to manipulate the power provided to the core. Sensors were used to measure the current and voltage into the heaters. As the tests evolved, a Variac controller was added to improve precision, reducing the number of control zones to three. The heat pipe calorimeter thermocouples were used to calculate the power transferred by each heat pipe using the mass flow rate, specific heat, and water temperature rise. Figure 22 shows the overall setup as it looked prior to testing.

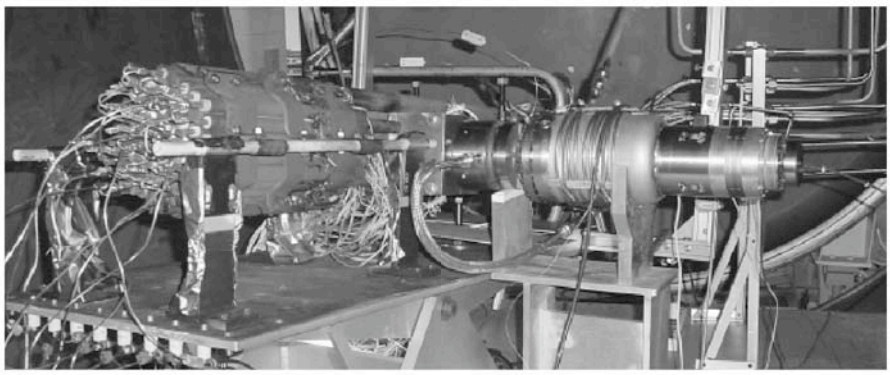

Figure 22. Overall setup of the SAFE–30 core before test.

3.3.1 Test Description

A total of 29 tests were performed using the SAFE–30 setup; however, eight of these tests were restricted to examining an individual module. During each test, new lessons were learned and these results were implemented in the next test in an effort to minimize potential problems and maximize the ability to mimic an actual nuclear test. Table 4 summarizes each test, its conditions, and interesting conclusions. The first tests were performed in a hard vacuum environment with three simulated heat pipe failures; a worst-case scenario was used to improve overall understanding with few problems encountered.

Initial trouble involved incorrect electrical contact between heater units and the heat pipe modules, resulting in a short-circuit condition, which terminated a test. The condition was resolved and heaters were able to reach and maintain a higher operating temperature. However, the ability to run at higher sustained temperatures resulted in a new problem for the industry-available heaters. The manufacturing process for the industrial heaters allowed gas to be trapped; this gas would expand at high temperatures, resulting in failure of the heater units. This situation was resolved by using MSFC in-house heaters being developed under a research program to support the upcoming SAFE–300 test series. All heaters in the SAFE–30 core were replaced with MSFC-manufactured heaters, which could withstand the temperatures and test duration. A new power supply and only two simulated failed heat pipes were used. After configuring the heaters and power supply, test 7 ran successfully at hard vacuum, accumulating ≈18,000 s of operation. This test is discussed in detail in section 3.3.3.1.

With completion of the vacuum tests, the next step was to replicate the Mars atmosphere by conducting the test in an appropriate CO_2 environment. The two initial tests failed—test 8 produced inconsistent data, and test 9 was terminated because of a short-circuit condition due to chamber leak. The system was repaired and test 9a was performed successfully, producing steady-state operation data within a CO_2 environment. Test 9a is discussed in detail in section 3.3.3.2.

A question had been posed regarding the degree of coupling between the calorimeters and the heat pipes. If this coupling were poor or inconsistent, the extracted power per heat pipe would be low and highly variable. This led to a number of tests using an individual module to determine how coupling

could be improved. Several tests were performed examining combinations of stainless steel mesh material, Cu sheathing, and a graphite blanket. The results of these tests concluded that the Cu sheathing material wrapped around the heat pipe provided the best overall coupling. Figure 23 shows a closeup of the core/heat pipe/calorimeter with some of the Cu sheathing material exposed on the actual test.

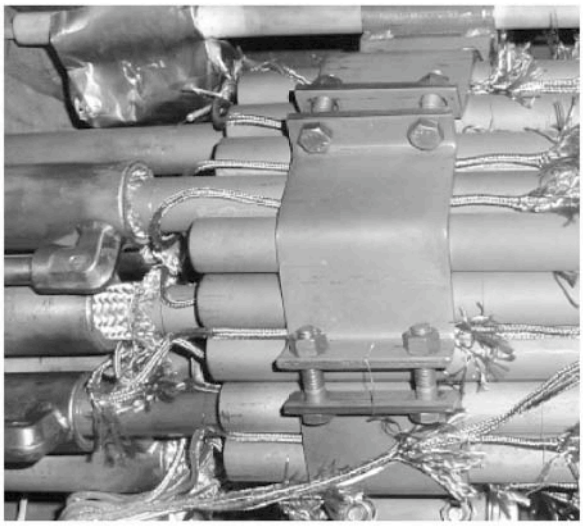

Figure 23. Implementation of modified calorimeter.

After the Cu sheath technique was implemented into the standard setup, additional testing was performed using test 19 with a setup similar to that used on test 9a; test 19 ran without incident.

The next test sequence involved attaching a Stirling engine to the heat pipes. The first several tests experienced difficulty in starting the Stirling engine, even at ambient pressure conditions. It appeared that the balance motor was having trouble starting; to determine the cause, a number of troubleshooting tests were performed. To aid in these troubleshooting tests, heaters were placed directly into the heat exchange locations used to transfer energy from the heat pipe to the Stirling engine. The engine was started, indicating that sufficient heat was being provided. However, some vibrations were still present, resulting in heater movement and eventual shorting of the power leads. The layout was reconfigured slightly and heat pipes reinstalled into the Stirling engine heat exchanger for testing in a CO_2 environment. The Stirling engine was successfully started and data collected showing reasonable temperatures and power. Table 4 summarizes the testing series.

Table 4. Summary of SAFE–30 tests from September 15, 2000, to February 26, 2001.

Test No.	Date	Time Length of Acquired Data	Conditions Under Which it was Tested	Results/Interesting Conclusions
1	Sept. 15, 2000	No data on record	Vacuum environment; no calorimeters present; three simulated failed HPs near the middle	First test; getting a feel for the procedures using heaters and HPs; fuses blew due to wire contact
2	Sept. 20, 2000	12,891 s	Same as above	Repeated test 1 with same hex configuration but a heater blew after higher temps were reached
3	Sept. 21, 2000	Data file lost during test, ≈18,000 s long	Same as above	Replaced bad heater; repeated test 1 with same hex configuration but a heater blew again, so a different type of heater will be used next time
4c	Oct. 19, 2000	5,395.3 s	Vacuum environment; with calorimeters attached; two simulated failed HPs on the outside surface	New configuration, new heaters, and new power supply used for the next few tests; warmed up past 300 °C until fuses blew
5c	Oct. 20, 2000	9,570 s	Same as above, same configuration, added a Variac power supply controller	Used Variac power supply to take care of blown fuse problem, rewired and it reached the maximum amps (56) with no problems
6	Oct. 23, 2000	3,431 s	Same as above, same configuration	Removed Variac and continued to run the single phase to the voltage controllers, but fuses blew again
7	Oct. 24, 2000	17,706 s	Same as above, and rewired Variac onto setup again, repeat of test 5c	Most successful test so far; peaked nicely and slowly dropped in temperature
8	Nov. 8, 2000	34,711 s	CO_2 environment; with calorimeters; same configuration for both working and failed HPs	Same as test 4c only in CO_2; longest test run so far; power input versus power output not good
9	Nov. 14, 2000	19,154 s	Same as above, except an additional controller was added for better control; the core was insulated for improved heat transfer in the core	The test ran fine, but there was a slow leak in the chamber and so it caused the fuses to blow
9a	Nov. 14, 2000	13,233 s	Repeat test 9 ensuring no leakage	Successful test; reached a fairly good steady state in the middle
10–18	Nov. 22, 2000, through Dec. 1, 2000		These tests were done on a module only at a different location, so that they could determine the best possible way to couple the HPs to the calorimeters for improved conductivity. Finally a copper mesh/sheath was determined to work the best.	
19	Dec. 7, 2000	27,749 s	Same as test 9a except the core not insulated and the calorimeters were new prototypes; the goal was to maximize heat transfer from the calorimeters	Heat pipes were brought to 700 °C, then the CO_2 was introduced; the test ran well, good power reached and consistent temperatures overall
20	Jan. 17, 2001	1,258 s	The Stirling engine was attached to three of the heat pipes via a copper block. Individual controllers were used for each HP put in the Cu block. Ambient conditions, no core insulator again	The balancer motor was turned on but the Stirling was not able to start, even with a "kick start" attempt
21	Jan. 18, 2001	4,646 s	The Stirling engine was attached again, heater tape was put around the heater head of the Stirling at ambient conditions	The Stirling was given a "tap" with a hammer and began to run
21a	Jan. 18, 2001	8,747 s	The Stirling was attached and heaters were put in the Heat exchanger, instead of HPs, at ambient conditions	The Stirling engine was again jump started with the balance motor, but the vibration caused the heaters to shift, touch the block, and short out
22	Jan. 23, 2001	6,389 s	Stirling was attached again to HPs; there was one controller for the three Stirling HPs and one for the rest of the core, operated at ambient conditions	At 300 °C it wouldn't start, as well as with balancer motor. Then applied 6V to alternator and it started, but vibrations caused heaters to back out and short
23	Jan. 24, 2001	13,166 s	Heaters were installed again into the Stirling heat exchanger to determine the ability of the Stirling to start on its own, operated at ambient conditions	The engine started at ambient conditions with the balancer motor help, but the balancer motor fuse blew, shutting off
24	Jan. 26, 2001	5,567 s	Heaters are still inside the heat exchanger, but the Stirling and shielding were rewired to try to get the Stirling started better than previous times	The engine started so later the environment was vacuumed down to test in vacuum, and it ran with little vibration
25	Jan. 31, 2001	21,066 s	Stirling attached, begins in ambient conditions and once it runs; CO_2 is bled in	Runs between 450 and 600 °C from the Cu block to the heater head, depending on input power
26	Feb. 1, 2001	14,245 s	No additional extraneous backgrourd information has been given for this test case	Overall calorimeter and temperature trends are seen again in this test
27	Feb. 9, 2001	12,713 s	No insulators used for the core or the heat exchanger, but a new heat exchanger design is used; CO_2 environment	Started engine in CO_2, but power was cut off for ≈500 s as data shows, but steady state was achieved
28	Feb. 21, 2001	19,931 s	A shield was attached around the connection between the Stirling and the new heat exchanger to cut down radiation losses; otherwise repeated test 27	Stirling again kick starts in CO_2 environment. Slowly increase power by Variac and controllers until temps increase a bit, then let sit at steady state a while
29	Feb. 26, 2001	4,627 s	Purpose to obtain a good set of steady-state data in the CO_2 environment, so Stirling was removed and heaters rewired, core was shielded in this test	Bleed in CO_2, increase power and the center was noticeably hotter than the edges; core remains at an average of 675 °C for steady state, then cools down

3.3.2 Heat Transfer Computer Model

A FORTRAN computer code, specifically written to evaluate HPS cores, was used to interpret the test results by modeling the three-dimensional conduction and radiation via finite differencing. The code predicts both maximum and average module temperatures at any specified time given the input power, temperatures from each heat pipe, and other imposed conditions/geometries for the actual test. The model uses temperature-dependent properties of each material to calculate steady-state temperatures while accounting for the environmental boundary conditions: vacuum condition (test 7) and CO_2 condition (tests 9a and 19). The model also accounts for the use of insulator material placed around the core assembly (test 9a). The model can be manipulated to predict performance with any number of failed/working heat pipes and the effect of using various clad materials, fuel compositions, and fill gases. Additionally, factors such as the conductivity between the fuel pellets, clad, heat pipes, and the modules, along with emissivity for the clad and radial reflector can all be varied to adjust for actual test conditions, improving agreement. The FORTRAN model demonstrated sufficient versatile in assessing temperature distributions for the resistance heated core, directly applicable to an actual fission-heated system and adjusted to account for different characteristics. A limitation within the model architecture is the relatively course mesh, which has only six azimuthal nodes per tube/heat pipe; it is uncertain the level of error this induces into the calculations. The model has since been modified to allow nearly unlimited discretization in all three dimensions; this study may be reperformed with this improved version of the code or another more detailed model when developed.

3.3.3 Data Analysis

Tests 7, 9a, and 19 were the most successful runs in terms of producing usable data. In each case, a thorough analysis will be performed, demonstrating the heat transfer characteristics of the system. Unfortunately, for each of these tests, there were only 10 working modules (heat pipes). One module was damaged during shipping—the fill stem was damaged, resulting in a loss of weld integrity—and a second module was destroyed when a heater electrically short-circuited against it during a preliminary test.

Thermal losses from the SAFE–30 to the surroundings were difficult to predict and routinely quantify, especially since it was not a top priority to control the radiation/conduction losses for this initial set of experiments. Therefore, boundary conditions, such as surface emissivities, were set empirically based on the test data. In most cases this represented only a minor change from predicted values. The analysis proceeded in the following manner. First, the heater power, heat pipe temperatures, and test environment conditions were input into the code. If the calculated heat pipe power was lower than the measured values, the core losses were reduced by decreasing surface emissivities in the model, and vice versa. This process continued until the power output predicted by the code achieved an acceptable match with the measured power output, typically required only minor tweaks. When this process was complete, module temperatures were compared in two ways. First, the maximum temperatures recorded for each specific module in the actual test were compared to the calculated maximum module temperature from the code. Second, an average temperature was calculated from the recorded thermocouple temperatures—averaging was used to reduce the effect of possible faulty thermocouple readings. This average temperature was then compared to the average module temperature generated by the code. Figure 24 shows the consistency of the thermocouple readings, comparing

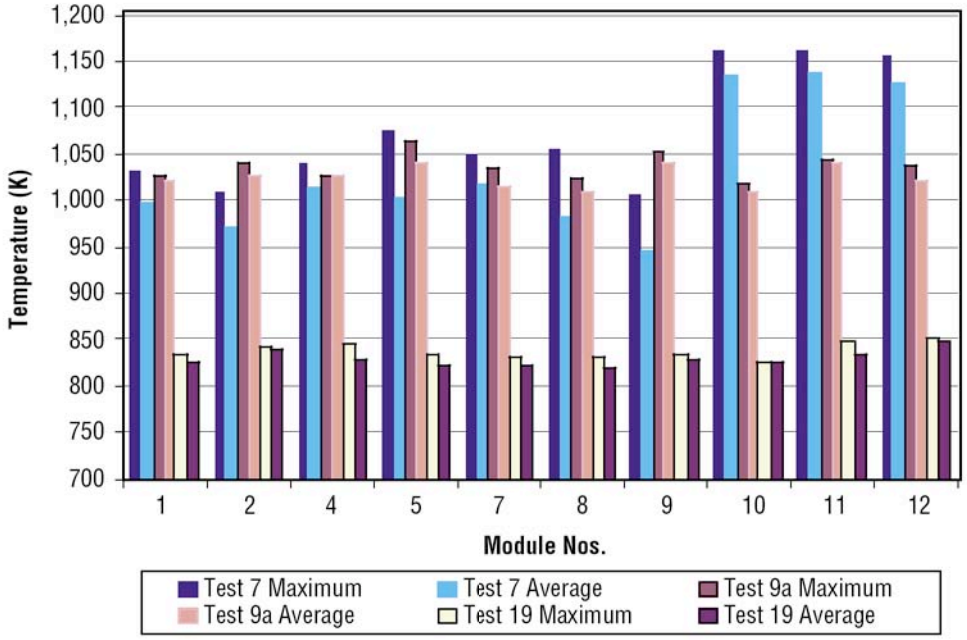

Figure 24. TC readings for representative tests.

maximum module temperatures to the average values. As can be seen from these data, the variation in the temperature readings is minimal, a good indication of consistent core heat transfer and thermocouple readings.

The power input to the heaters was calculated using the data recorded from each control zone. Each zone controller measured the voltage (in volts) and the current (in amps), allowing the power (watts) to be calculated as

$$P = I \times V \ , \tag{4}$$

where P is power, I is current, and V is voltage. Total power was assessed as the sum of all individual zone calculated powers. The power output through the heat pipes was determined using the fundamental heat transfer into the calorimeter cooling water as

$$Q = \dot{m} \times c_p \times \Delta T \ , \tag{5}$$

where Q is the power, $\dot{m}$ is the mass flow rate of the calorimeter cooling water, c_p is the specific heat of water, and ΔT is the change in the water temperature across the calorimeters. The mass flow rate was measured using the 0.75-in flowmeter and the density of water was assumed to be 1,000 kg/m^3. After calculating each individual calorimeter power, they were summed to obtain the total power output; however, the power from the two damaged modules was essentially zero.

As the evaluation of the data proceeded, it was noticed that the computer model was consistently underpredicting temperatures. The error was linked to ≈20 K difference between the actual thermocouple reading and the heat pipe wall temperature within the core (a parameter used in the heat transfer code). A steady-state conduction/radiation calculation indicates that a 5–15 K temperature drop

occurs between the thermocouple spot weld and heat pipe outer wall. This ΔT depends on how well the thermocouple is bonded to the heat pipe. In addition, another steady-state conduction calculation showed a temperature drop of ≈5 K through each of the internal heat pipe sections: stainless steel heat pipe wall, Na annulus, and the wick. Finally, there is another temperature drop of ≈5 K between the heat pipe wall within the core because the inner wick temperature is the same in the evaporator and condenser regions. Consequently, there is ≈20 K difference between the thermocouple reading and actual heat pipe wall temperature within the core, the latter of which is input into the computer model.

3.3.3.1 Test 7. Test 7 was conducted in a vacuum environment. Figure 25 shows the relationship between the power input through the heaters and the power taken out through the calorimeters. Information about where the possible losses could have occurred will be discussed later. Figure 25 shows that the power output follows the step changes in power input very well until the power approaches 10 kW. As the power is increased further, losses from the core to the surroundings begin to dominate as the core was not insulated. Figure 26 shows the temperatures for one-third of the core that does not contain a failed module. It behaves as would be expected; all of the heat pipes are significantly cooler than the actual modules. Also, the heat pipe and module temperatures in the center (module 10) are the highest.

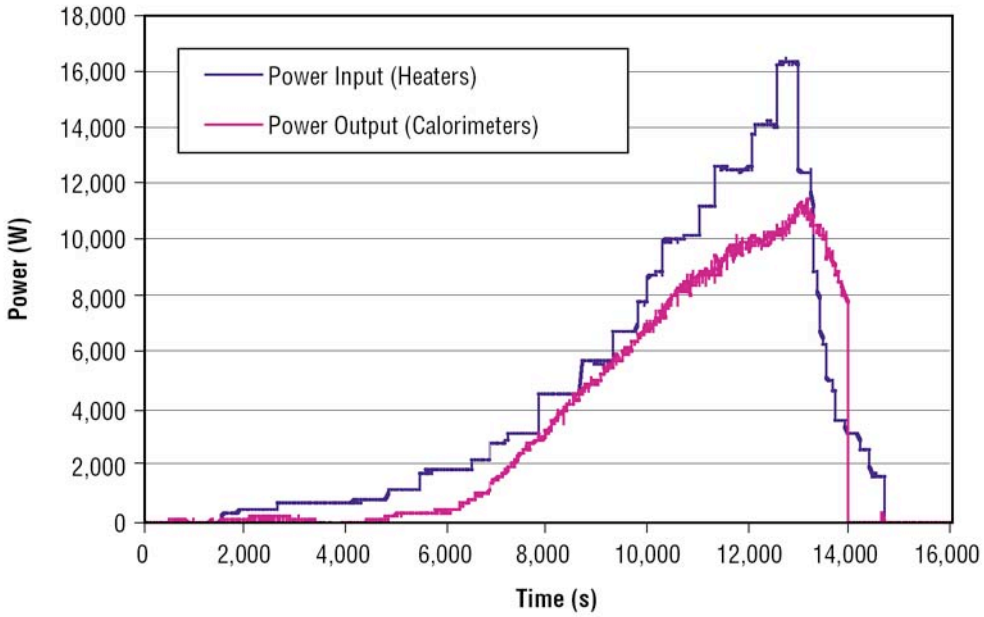

Figure 25. Power input versus power output for test 7.

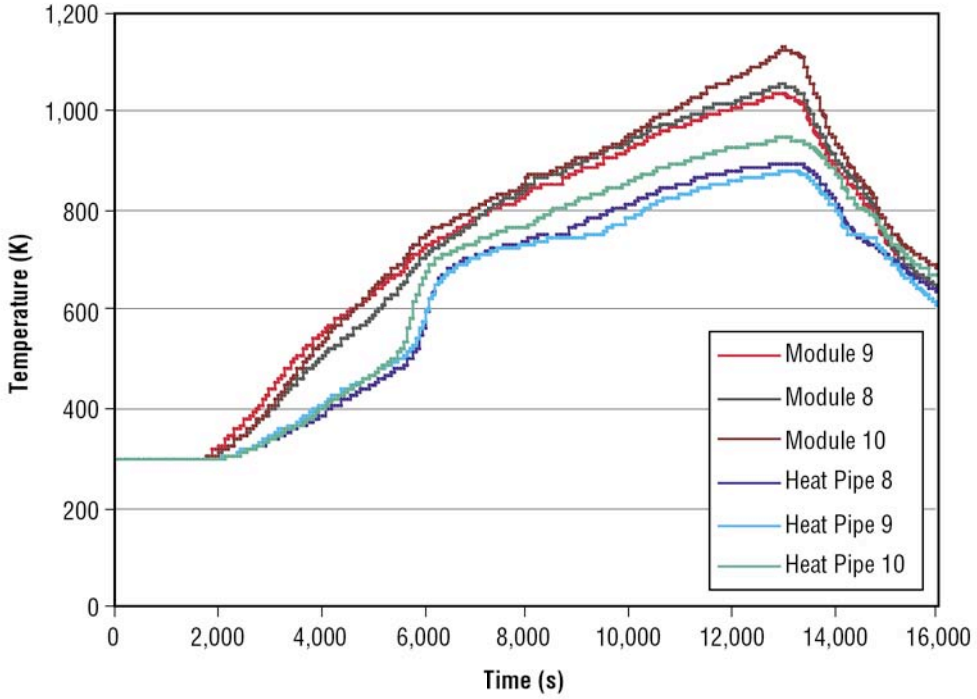

Figure 26. Heat pipe and module temperatures for test 7.

The vacuum case was the most difficult to duplicate with the heat transfer code. One potential reason for this difficulty may relate to the lack of a prolonged steady-state interval in the data (flat portion in the temperature profile); the actual test temperature was constantly changing. It was decided that a time slice near peak temperature would be best suited for modeling purposes. The data time stamp of 13,100 s was selected and all corresponding temperatures and boundary condition values were input into the model. The fuel type selected for the model was UO_2 because it has a lower conduction compared to UN fuel, so it imitates the test heating characteristics more realistically. The core layout was defined in the model as having two failed heat pipes (Nos. 3 and 6) with no fuel (no power deposition) in either module. Figure 27 points out the empty modules located in the SAFE–30 stack.

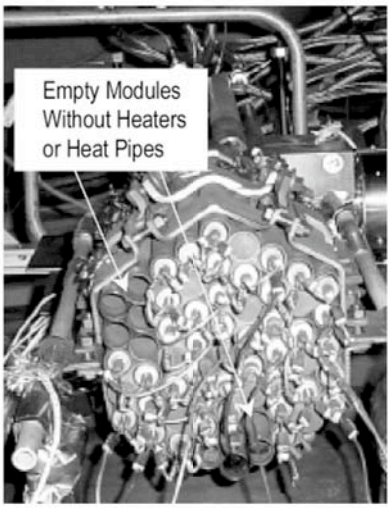

Figure 27. Locations of empty modules.

The results of these comparisons are reasonably good considering the roughness of the hardware setup. The overall percent difference between the measured maximum module temperatures and the calculated maximum module temperatures was 47.9 K (38.7-percent difference in ΔT). The overall percent difference between the actual average module temperatures and the calculated average module temperatures was 57.8 K (24.9-percent difference in ΔT). Figures 28 and 29 illustrate that individual module temperature compared favorably to those predicted by the model. The failed modules (3 and 6) are omitted from this comparison. The bar graphs also include maximum and average temperatures for each module heat pipe. The line in the middle of the graph shows the average heat pipe temperature at the time the data were taken. The largest discrepancy in these predictions is within the core inner modules (Nos. 10–12), producing temperatures nearly 100° higher than predicted. This discrepancy appears only in test results for setups that have a hard vacuum boundary condition.

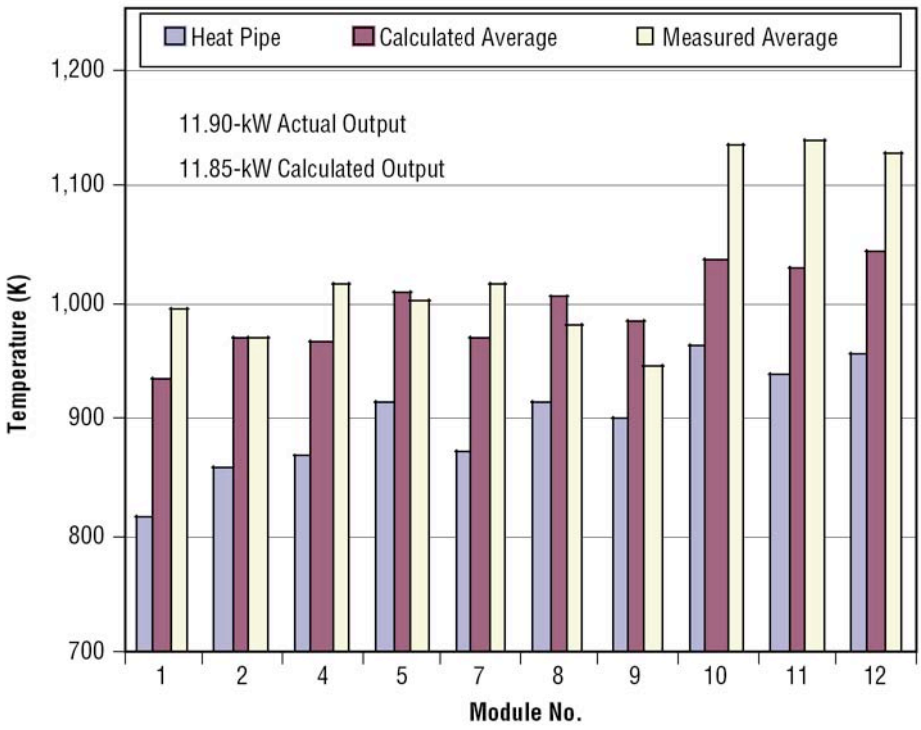

Figure 28. Comparison of measured and calculated average module temperatures for test 7.

Test 7 was the only hard vacuum boundary condition test that was studied in detail. This test also exhibited the largest difference between measured and calculated values. A possible reason for this difference stems from the lack of good values for surface emissivities. The vacuum condition increases the importance of radiative heat transfer; inconsistency in the surface emissivity data would produce significant variability, complicating the modeling effort. Despite this limitation, the overall comparison is still fairly good.

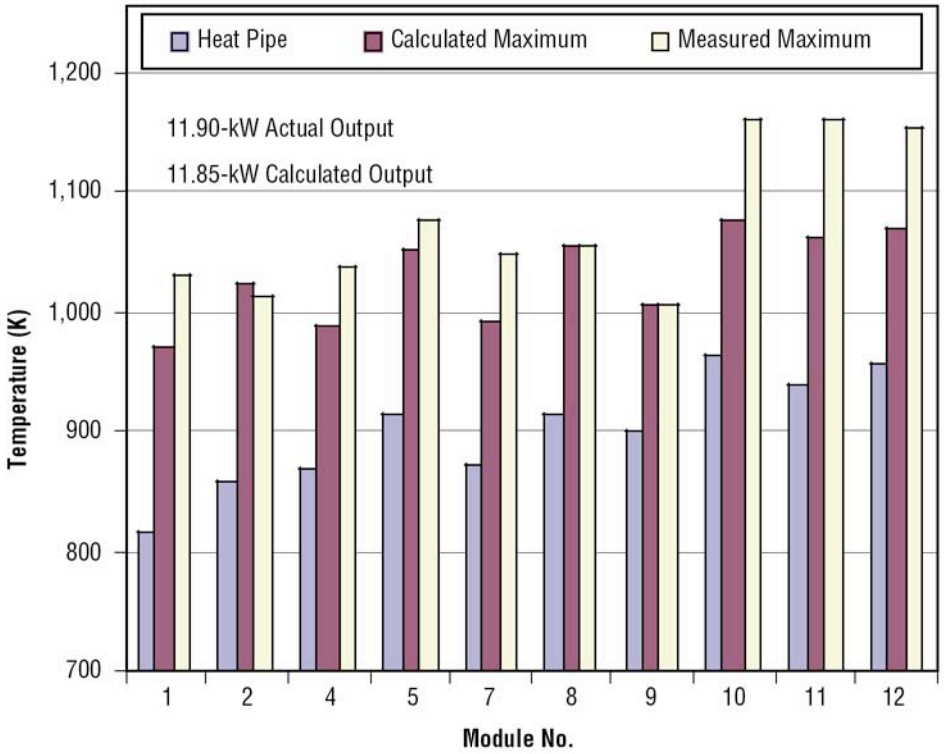

Figure 29. Comparison of measured and calculated maximum module temperatures for test 7.

3.3.3.2 Test 9a. Test 9a was conducted with a background environment of 0.2 psi gaseous CO_2 and made use of nearly the same hardware configuration and test procedure validated in test 7. The test duration was 13,233 s and reached a maximum power of ≈12.4 kW as measured by the calorimeters. The vacuum chamber in which the test was conducted was initially evacuated to provide an inert environment and then later backfilled with CO_2 to the desired pressure after initial power up was completed. The initial powerup phase (under hard vacuum) was completed in ≈3,500 s (core reached maximum power level), at which time CO_2 was introduced. Test 9a was unique in that a circumferential insulating shield was added to the perimeter of the core in an attempt to reduce radiative losses. Figure 30 shows an image of the installed insulation band with the core at ≈900 K; the ends still have significant radiation losses. This test is analyzed in detail at 4,300 s during a steady-state portion of the run. The power input versus power output is illustrated in figure 31. The drop in power, when CO_2 was introduced, was necessary to keep applied heater voltage low, minimizing the chance of gas breakdown. This figure graphically demonstrates the difficulty experienced to date in thermal coupling the heat pipes to the calorimeters under vacuum conditions (the inefficiency of radiation coupling). When CO_2 is introduced into the vacuum chamber, the coupling across the small gap between heat pipe and calorimeter becomes conduction dominated, resulting in the majority of the core input power being transferred more efficiently to the calorimeter (a desirable effect).

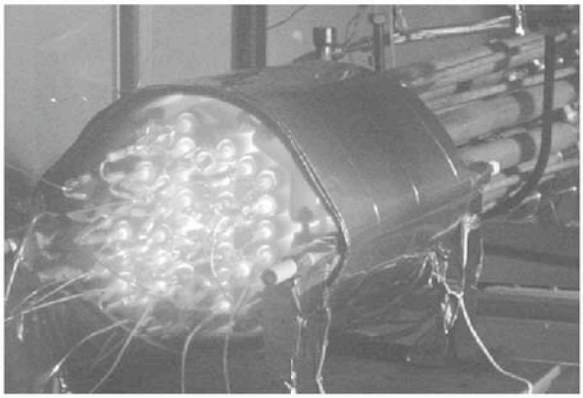

Figure 30. Test 9a core with insulation.

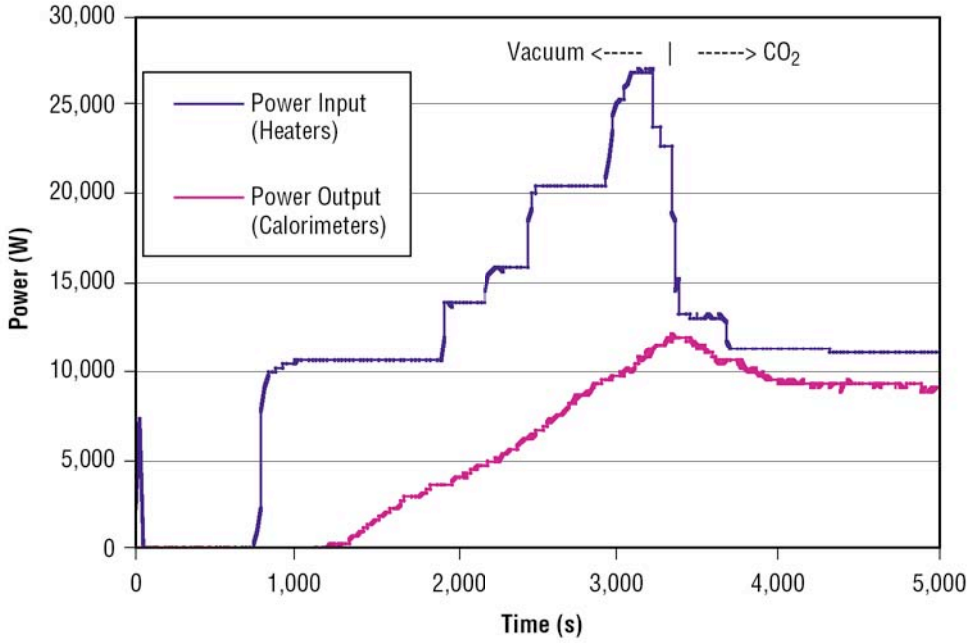

Figure 31. Power input versus power output for test 9.

Figure 32 shows the recorded temperatures of each individual heat pipe throughout test 9a. Since heat pipes 3 and 6 simulate failed units (nonworking straight tubes), these units show the lowest temperatures. The temperatures of the working heat pipes are relatively uniform in the CO_2 environment with a spread of 100 K when compared to the previous noninsulated hard vacuum tests which produced spreads in excess of 200 K.

The presence of the CO_2 and insulation material has significantly improved the ability of the model to predict experimental results. The overall percent difference between the actual maximum module temperatures and the calculated maximum module temperatures was 28.8 K (a 24.4-percent difference). The overall percent difference between the actual average module temperatures and the calculated average module temperatures was 3 K (27.4-percent difference in ΔT). Figures 33 and 34 show the calculated and average temperatures for each module.

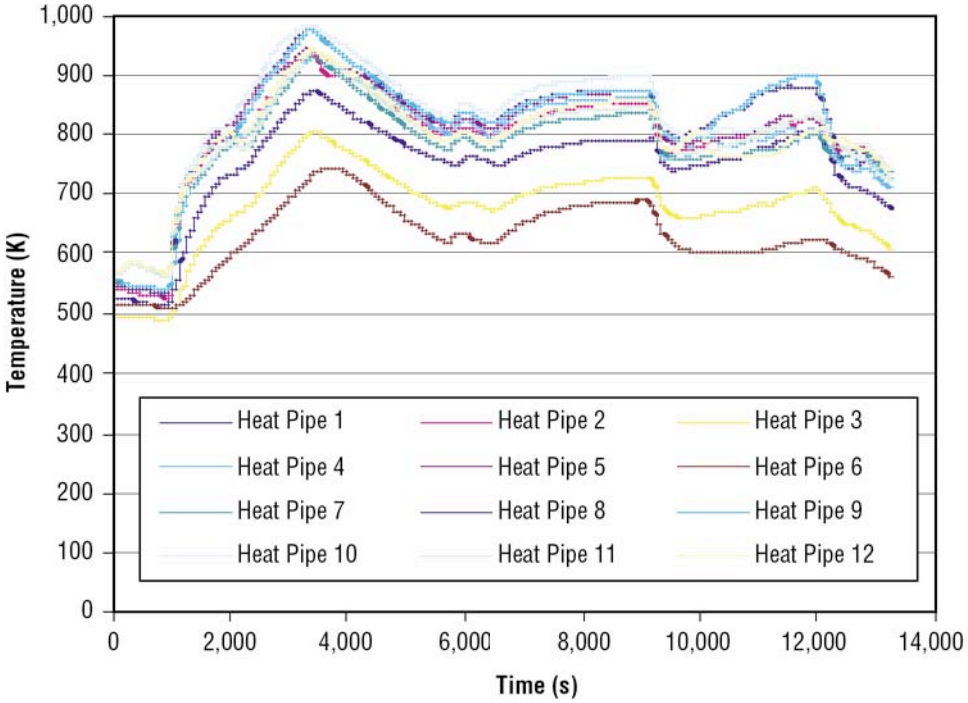

Figure 32. Heat pipe temperature during test 9a.

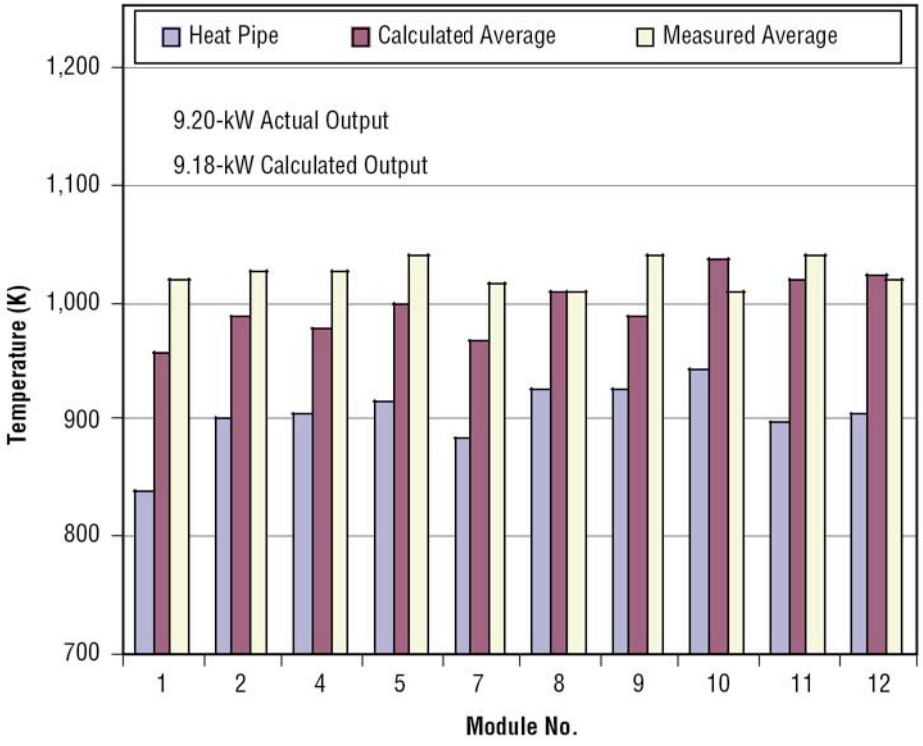

Figure 33. Comparison of measured and calculated average module temperatures for test 9a.

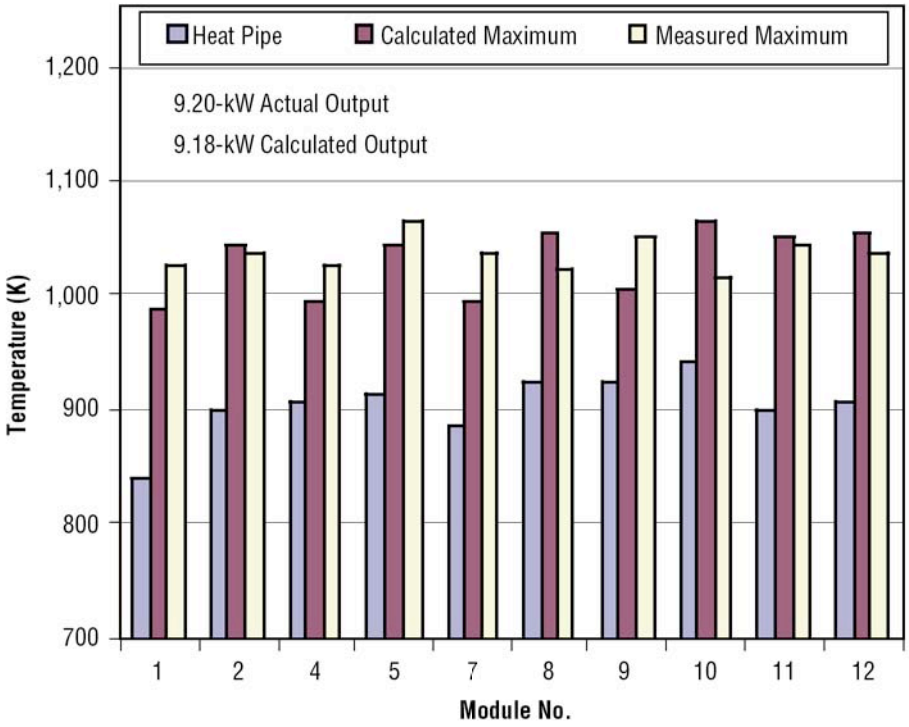

Figure 34. Comparison of measured and calculated maximum module temperatures for test 9a.

3.3.3.3 Test 19. Test 19 was also performed in a CO_2 environment; however, the core circumferential insulation shield (used in test 9a) was removed. This test took advantage of a single module study with a goal of determining how to better couple the heat pipes with the calorimeters. As a result, a compressible wire mesh (used in radio frequency (RF) shielding and grounding applications) was placed between the heat pipes and the calorimeters (fig. 23). With the presence of the CO_2 fill gas, this allowed very good coupling and good agreement in transferred power during steady state.

This test was the record setter for the entire test series, achieving maximum values for both temperatures and powers. The maximum heat pipe power reached was 19.2 kW; had all 12 modules been operational, this would have translated to a throughput in excess of 23 kW. A primary goal of this test was to achieve an extended period at constant power, ensuring a usable steady-state interval for numerical evaluation. The detailed analysis of this test was performed at a data time stamp of 20,000 s. During this period, losses were minimal due to the low power setting. Once again the CO_2 was introduced into the vacuum chamber, similar to test 9a, after the initial powerup was completed (≈11,000 s). Figure 35 shows the power input versus power output, highlighting the long steady-state interval used to correlate test data with model predictions.

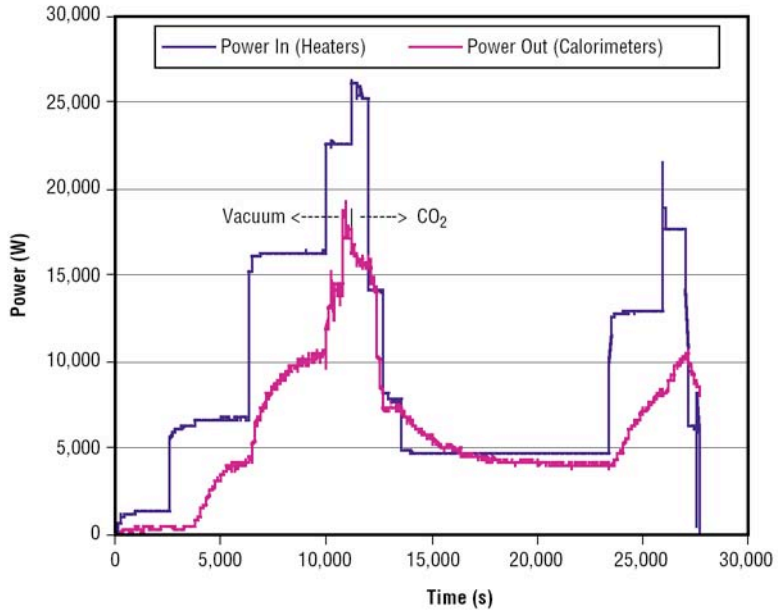

Figure 35. Power input versus power output for test 19.

The input parameters used in the numerical model were similar to those used in test 7 with the exception of a background thermal conductivity simulating a CO_2 environment rather than in hard vacuum. The final temperatures predicted by the numerical model agree with the recorded test data exceptionally well. The maximum temperatures calculated were 16.6 K different from the actual temperatures (34.4-percent difference in ΔT). The average temperatures calculated were only 12.6 K different from the actual recorded average temperatures (24.4-percent difference in ΔT). These results are shown for each module in figures 36 and 37.

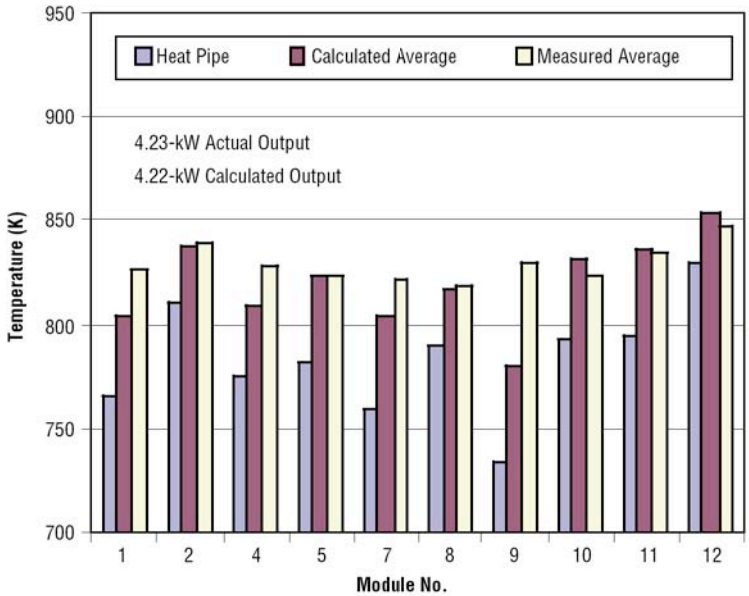

Figure 36. Comparison of measured and calculated average module temperatures for test 19.

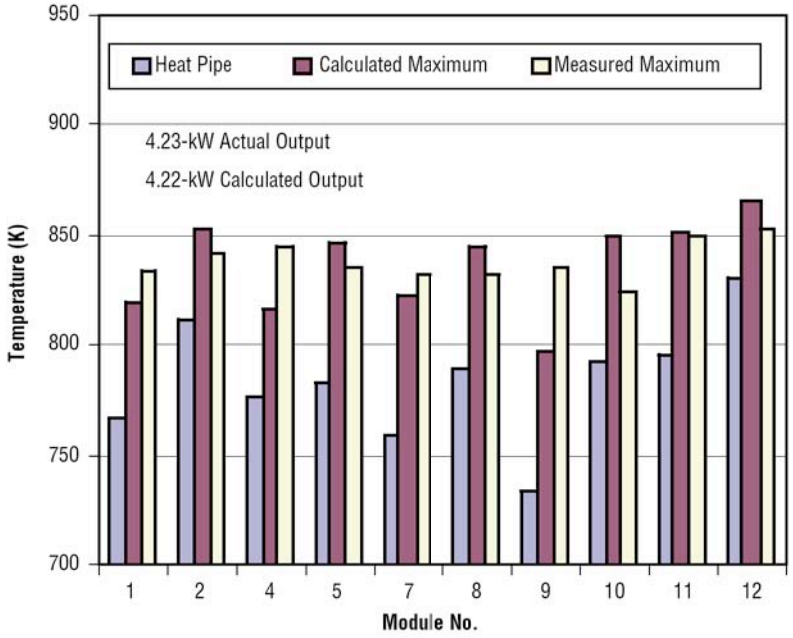

Figure 37. Comparison of measured and calculated maximum module temperatures for test 19.

A detailed comparison was also done at the peak heat pipe power (19.2 kW), the highest power obtained during any test. Discussion of this case is included in table 5.

Table 5. Summary of each test that was studied in detail.

Parameters Measured During Test	Test 7	Test 9a	Test 19	Test 19 Maximum
Time (s) at which test data was studied in detail	13,100	4,300	20,000	10,858
Testing environment	Vacuum	CO_2	CO_2	CO_2
Conditions of the core	Not insulated	Insulated core	Not insulated	Not insulated
Power input (kW) through the heaters	12.4	11.3	4.7	22.7
Power output (kW) through the HP calorimeters	11.9	9.2	4.23	19.2
Maximum HP temperature (K)	944	922.8	810.7	968.9
Module No.	10	10	12	8
Maximum power (kW) out of one module	1.51	1.16	1.08	3.07
Module No.	2	8	4	8
Maximum module temperature (K)	1,167.7	1,073.4	852	1,300.6
Module No.	10	3	12	2
Maximum average module temperature (K)	1,138.7	1,041.6	847.8	1,292.9
Module No.	11	9	12	2
Average difference between calculated and measured module ΔT (K) (peak TC location)	47.9 (Δ 24.9%)	28.8 (Δ 24.4%)	16.6 (Δ 34.4%)	52.3 (Δ 18%)
Average difference between calculated and measured module ΔT (K) (average of TC locations)	51.8 (Δ 38.7%)	34 (Δ 27.4%)	12.6 (Δ 22.4%)	88 (Δ 30.4%)

3.3.4 Thermal Losses

The final aspect of these tests is to address the overall thermal losses. Theoretically, the difference between the input and output power can be accounted for in the thermal losses through the noninsulated sections of the core (the front, back, and sides) and the structural attachment points. Figure 38 shows an example of the large uninsulated surface area of the SAFE–30 core block. In an effort to quantify these losses, radiation heat transfer rates were calculated. Test 7 was examined in detail in an attempt to quantify these losses in a precise, analytical way. This process was initiated by calculating the average fuel tube temperature for the modules using the thermocouple readings closest to the heaters. Based on radiation heat transfer, the heater temperatures can be calculated. The equations are as follows:

$$Q_{tube} = Q_{total\_input} / 40 \ , \tag{6}$$

since there were only 40 heaters in the core; then:

$$Q_{tube} = A\sigma\varepsilon(T_{heaters}^4 - T_{tube}^4) \ , \tag{7}$$

where Q_{tube} is the heat flux or power from each individual heater tube, A is the surface area of the heater tubes, $T_{heaters}$ is the temperature of the heaters, σ is Boltzmann's constant, and ε is the emissivity of the stainless steel; 0.6 was used in all cases as the surfaces were blackened due to CO_2 exposure at high temperature. Using the actual heater temperatures, the radiation losses from the heater (core back) side can be calculated. The power loss from the core's perimeter acreage was determined using an average temperature for the surface area (based on thermocouples) and radiative heat transfer. Figure 39 illustrates the individual power losses and calorimeter power transfer in reference to the total input power provided to the core assembly (based on output from the power controllers). The power balance agrees extremely well, given the simplicity of the evaluation.

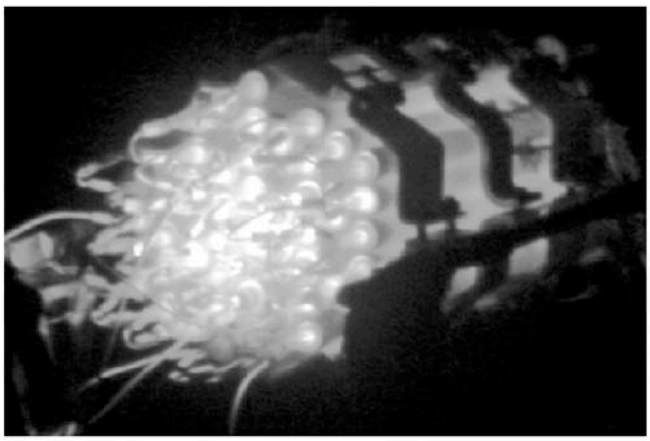

Figure 38. Core during test.

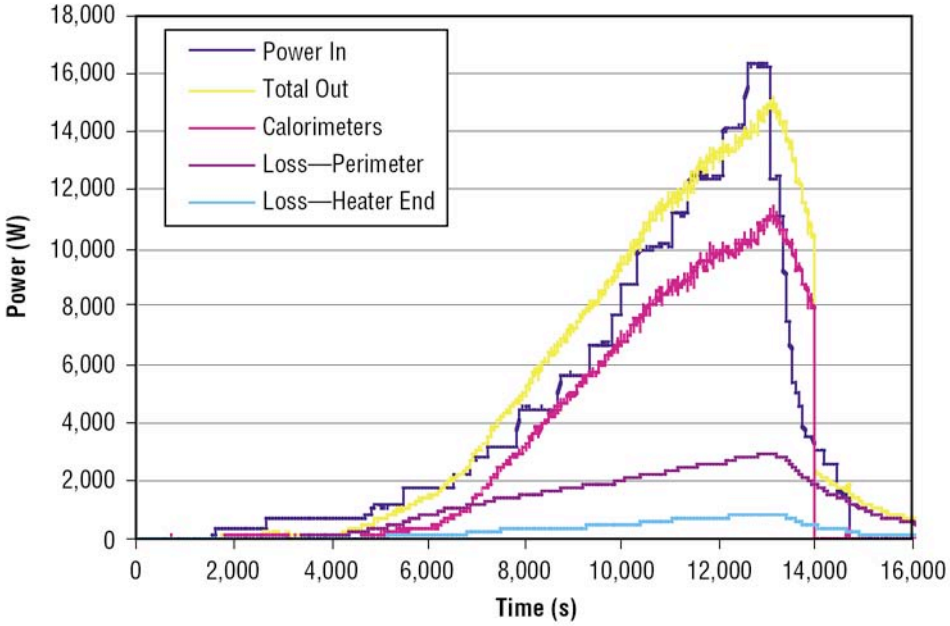

Figure 39. Individual losses, summation of losses, and total heater input (calculated from controllers).

3.3.5 Conclusion

Overall, the SAFE–30 resistance heater test series was a success. A significant number of tests was completed, generating a great deal of lessons learned from hands-on experimental iterations. In the end, a reasonable set of test data was completed with ample proof that from a thermal and stress standpoint, the HPS would work in both the Mars- and space-based environments. The tests and analysis covered a broad range of temperatures and powers. Table 5 summarizes each test that was discussed in this TM.

The last two rows of table 5 quantify how well the experiment results compare to the numerical models assessment. This comparison is based on the temperature difference between the module clad and the heat pipe, the most important parameter in modeling the heat transfer. The relative difference between measurements and calculations is generally between 20 and 30 percent. There are a number of possible reasons for this difference:

(1) Inaccurate thermocouple readings due to variations in bonding and unwanted contact with adjacent surfaces.

(2) Significant thermal losses with a wide range of variability, especially radiation.

(3) Limitations in the heat transfer model, particularly related to heat transfer across the fuel pin (UO_2 versus the inefficient radiation coupling between a heater and clad).

(4) A general level of error expected due to the lack of regiment imposed on the overall test procedure; tests were performed rapidly due to cost and schedule limitations.

(5) Uncertainties in modeling parameters, such as emissivity, thermal conductivity, and braze wetting fraction.

These results are sufficiently accurate to draw the conclusion that heat transfer within the SAFE–30 system is highly predictable. Many of the areas that contributed to the inaccuracies have been identified and can be avoided in designing future tests.

Although the peak power measured by the calorimeters was only 19.2 kW, this does not mean that the SAFE–30 could not produce its intended 30 kW. First, there were only 10 working modules; 12 modules would have immediately increased this value to over 23 kW. Second, the thermal coupling between calorimeters and heat pipes was never adequate, limiting the power that the calorimeters could extract. Third, and most important, the heaters did not provide a prototypic conduction path across the fuel pins, limiting redistribution of heat, causing a substantial increase in module temperatures as compared to an actual nuclear system. Last, the failure to protect against large thermal losses at high power settings made it increasingly difficult to exceed 20 kW. Calculations show that if these limitations were corrected, the SAFE–30 would easily have produced power levels in excess of 30 kW.

The SAFE–30 tests provided an overview of the general techniques, environments, and hardware used to simulate the heat transfer within a nuclear core. The later tests, which implemented the Stirling engine, were completed to demonstrate that an HPS is a realistic concept that can provide power for future space applications. A primary goal was to demonstrate the use of a heat transfer computer model to reliably predict the operations of a system such as SAFE–30 resistance heater tests. The initial results indicate that the model was able to predict behavior, even with less-than-textbook test conditions, demonstrating the overall capability of the program. In general, the tests indicate that the SAFE system is a robust, near-term, low-cost, simple system that works. Last, the SAFE–30 resistance heater tests were one successful step along a path that promises to bring mankind closer to the ultimate goal of understanding and routinely exploring the depths of outer space.

3.4 Lessons Learned

Some of the technical lessons learned from this experimental test program that are directly applicable to the nonnuclear testing of any core included the following:

- There may be vibration issues associated with component startups; e.g., energy conversion, electric propulsion engine, etc. These can easily be addressed through proper support structure designs.

- Matching prototypic power and control zones are no trivial matter. While it is possible to provide the core with a total power, trying to accurately match the radial pin power profile with accuracy, while simultaneously being nonobtrusive to the test article, was difficult. This can be accomplished through an automated integrated power and control system. However, this system must be designed to give flexibility of being reconfigured easily to test any core configuration that is designed to be nonnuclear tested. In order to avoid voltage breakdown, this automated and integrated power system must also be able to operate at extremely low voltages; e.g., <160 V, for GHe in the vacuum chamber.

- The hookup of heater units to a test article is an "art." For future cores, the hookup must address all of the following issues simultaneously: hundreds of heater junctions in a circular footprint with <12-in diameter, axial power profiles, temperatures in excess of 1,000 °C, test periods in excess of 8 hr, multiple startup/shutdown cycles, hard vacuum/gas environments, and nonobtrusive connections to the test article.

- Moving from a laboratory environment with the MUTT to the SAFE–30 was a monumental step in every aspect of testing. The test article grew from 6 to 48 heaters, instrumentation requirements increase by two orders of magnitude, and the MUTT had no real integration issues; e.g., hooking up an energy conversion cycle to the core. Moving from the SAFE–30 core to the next heat pipe reactor concept shall also be a monumental step, as there will be four times as many heaters in the same aerial footprint, power control capability "on-the-fly" will be a necessity, and manufacturing issues will become apparent as parts begin to be more prototypic.

- This test series clearly shows that significant attention should be placed on isolating the thermal coupling between the facility hookup and the test article. Also, the test article should be connected to a power source that is separate from that used to operate the facility (eliminate crosstalk and improve safety).

- Develop better techniques for thermal coupling heat pipes and calorimeters/heat exchangers, must be emphasized for the follow-on SAFE–100 program.

- As the area available for instrumentation becomes smaller, such as interstices forming between modules/clads, and more difficult to access, such as with heat exchanger (HX) flow channels, state-of-the-art instrumentation techniques must be investigated to address temperature, pressure, strain, and bulk core deformation measurements.

- This test series demonstrated that certain aspects of fission system operation can be simulated using nonnuclear test facilities. Any future fission program whose goal is a flight system should investigate the use of nonnuclear testing where appropriate to significantly decrease programmatic cost. Data gained from such tests; i.e., failure testing and margin testing, may be more thorough since a great deal of the safety issues associated specifically with nuclear testing, such as hot cells, will not have to be addressed.

3.5 Future Testing

While the SAFE–30 demonstrated that resistance-heating techniques could be used for an entire core versus a module, it also shed light on issues that would be less expensive to solve by testing another stainless steel core, rather than moving directly to a refractory metal system. The refractory metal core pin size is half the size of the SAFE–30, making electrical hookup, power control, and heater design much more difficult than the SAFE–30. The SAFE–30 demonstrated that the heat exchanger design is best performed simultaneously with the core design, rather than discounting it completely. The SAFE–30 demonstrated only one possible technique—brazing—for module manufacturing. Finally, the SAFE–30 demonstrated the need to set up a mechanism to mass-produce heat pipes in a cost-effective manner.

The next core in the MSFC phase 1 heat pipe testing series is the SAFE–100. This core is designed to deliver 100 kW thermal power to the heat pipes and is constructed from 316 stainless steel using geometry similar to the SAFE–400 refractory metal design. Originally, the core was designed to be an exact geometric duplicate to the refractory metal core; however, a change in mission requirements altered the refractory metal core design during the manufacturing and buildup of the SAFE–100. All the lessons learned in the SAFE–100 are directly applicable to the updated refractory metal core design so building another "stepping stone" core between the SAFE–100 and the SAFE–400 is not anticipated. Keeping the lessons learned in the SAFE–30 in mind, the SAFE–100 is to accomplish the following specific objectives:

- Investigation of manufacturing techniques, such as HIP, for module and core assembly.
- Core support systems, including design and development of a flight-like prototypic core strapping structure.
- Provide updates to thermal codes, including modeling of appropriate insulation boundary around core to simulate radial reflectors, thermal performance, and thermal cycling effects (fatigue/strain).
- Design and fabrication of prototypic heat exchanger (from heat pipe to HX gas inlet).
- Demonstrate ability of prototypic heat exchanger to remove at least 90 percent of energy from heat pipes.
- Demonstrate ability of MSFC-manufactured heaters to provide sinusoidal temperature and power profile for over 75 tests. (Heaters are conservative due to radiative coupling and absence of conduction through heaters.)
- Demonstration of a 32 "hands-off" control zone system to match radial core power profile; heater design matches axial power profile.
- Development and demonstration of stainless steel heat pipe fill and capping capability at MSFC.
- Gain hardware-based insight into other required design attributes of more advanced space fission systems, including investigation of expansion characteristics for various core design options.
- Demonstrate ability of the core to efficiently transfer heat from the fuel elements to a point external to the core via heat pipes. Demonstrate a heat pipe transfer rate of >1 kW.
- Demonstrate performance of core heat pipe system operating in CO_2 at 6 to 12 torr (major constituent of Mars atmosphere).

While SAFE–30 demonstrated the brazing technique for module manufacturing, the SAFE–100 will use an HIP process. In designing the SAFE heat pipe reactor, it is highly desirable that the interstices between the fuel tubes and between the fuel tubes and the heat pipes are filled. The SAFE–30 modules were brazed together using a tricusp insert in the gaps between tubes to ensure maximum braze coverage. The SAFE–100 modules are planned to be diffusion bonded together using an HIP process. Although the complex geometry of the SAFE–100 is quite challenging to fabricate by diffusion bonding, it was considered worth the effort. If successful, the HIP technique will produce an assembly with the heat pipe completely embedded within the module and the module will have thermal conduction and strength equivalent to a solid structure. Although brazing was used very successfully for the SAFE–30, it does have some disadvantages: braze joints are not as strong as diffusion bonds, rarely provide 100-percent joint coverage, and are difficult to inspect nondestructively. Additionally, developing a satisfactory braze method for refractory metals will be quite difficult; whereas, once the mechanics of the HIP method have been successfully developed for the stainless steel SAFE–100, it should be fairly easy to transpose the tooling and methodology to a refractory system.

The SAFE–100 provides additional test data to better benchmark both thermal and structural codes as well as provide design guidance for the refractory metal core. The SAFE–100 analysis is based on a reactor core design, which assumes UN fuel with the small gap (between fuel and clad) filled with He. With this design, there is considerable potential for heat transfer through the fuel, which acts to reduce temperature gradients in the modules and attendant thermal stresses. In the nonnuclear test core, graphite resistance heaters are placed in the fuel channels. Although graphite is a good conductor, the tests are run in a vacuum, and there is little heat transfer across the gaps between the heaters and fuel clad. Because of the difference between the design core and test core, calculated peak temperatures and thermal stresses in the test core operating at 25 kW are approximately equal to those in the design core at 100 kW. The first few tests performed on the SAFE–100 (nonnuclear) will be at a 25-kW power level. Based on analysis performed for the test model, it is expected that the fuel clad will yield and undergo stress relaxation when operated at 100 kW, but that the plastic strains will be very small and well within the allowable strain range for SS–316.

4. END-TO-END DEMONSTRATOR OF THE SAFE, AFFORDABLE 30-kW FISSION ENGINE WITH A STIRLING ENGINE AND ELECTRIC PROPULSION ENGINE

To date, only a few electric propulsion concepts can support the high power requirements for future missions. Due to their specific impulse operating range, advanced ion and Hall thrusters are the most likely candidates to be used in the near term for a wide variety of missions spanning from low-Earth orbit to interstellar space. Depending on the mission scenario/profile, this efficient electric propulsion device can be powered by solar or space nuclear power. Beyond the use of these very efficient systems, mid- to far-term solutions might include propulsion concepts, such as the magnetoplasmadynamic thruster, the variable specific impulse magnetoplasma rocket, and the pulsed inductive thruster.

Research in the field of electrostatic acceleration has been conducted since the late 1950s, resulting in a number of different devices and ionization methods capable of supporting space propulsion. These devices use suitable grid electrodes for ion extraction/acceleration, converting electric energy to kinetic energy. The most commonly used ion source is based on electron bombardment where plasma is generated by electrons colliding with neutral gas. Thrusters based on the Kaufman concept use weak magnetic fields for ion/electron separation. To date, the most successful ion thruster developed by NASA is the NSTAR engine, which currently flies on board the Deep Space 1 spacecraft.

After an initial system's checkout of the core, heat exchanger, and Stirling engine, assembly was completed at MSFC. The assembly was shipped to the Jet Propulsion Laboratory (JPL) in Pasadena, CA, for attachment of the electric propulsion engine and final end-to-end testing. For this initial end-to-end demonstration of a nuclear electric propulsion system, the SAFE–30 power system was tested with a 15-cm-diameter ion engine. This small laboratory model engine was developed at JPL and incorporates several advanced ion engine technologies, such as carbon- (C-) carbon ion optics. The resistively heated reactor, Stirling engine, power conversion equipment, and ion engine were mounted in a 2.5-m-diameter by 5-m-long vacuum chamber. The 100-V output from the Stirling engine was converted to 1,000 V and used to accelerate the xenon ion beam. Because the output from the reactor/Stirling assembly was limited to 350 W, the ion engine discharge and neutralizer cathode was run with laboratory power supplies. Data from this test were used to help identify and resolve integration issues for future systems.

4.1 Safe, Affordable 30-kW Fission Engine Powertrain

The purpose of the end-to-end tests is to showcase the NEP concept by a simulated approach with inexpensive off-the-shelf materials in a relevant environment. An appropriate powertrain converts thermal energy mimicked by resistance heaters into kinetic energy. The end-to-end system demonstration consists of the SAFE–30 simulated core, 350-W Stirling engine, dc/dc converter, and 15-cm ion thruster with slotted C-C grids.

The power support system for the ion thruster consists of four separate power supplies providing power to the subsystems of the thruster, as described above. However, the power generated by the Stirling engine replaces the conventional beam supply. All other subsystems of the thruster will be maintained and controlled by the power support system. The powertrain between the Stirling engine and the ion thruster is illustrated in figure 40. The Stirling engine controller processes the generated power and provides logistics to the Stirling engine, depending on operating conditions and power demand (load). The control board algorithm manages the proper loading of the Stirling engine. Sensing circuitry monitors power demand at the output, and accordingly, the control board ties in or removes stages of a resistive load array. The ac power generated by the Stirling engine is processed by rectifier circuitry and converted to an output of about 123 Vdc and 3 A. The dc/dc converter steps up the input voltage of ≈123 Vdc to 1,000 Vdc with appropriate transformer circuitry. In addition, the device limits the inrush current during the startup sequence of the ion thruster. The inhibit switch is another important part of the converter, which is controlled by the power support system of the ion thruster. The switch terminates the high voltage provided by the converter to the thruster in case of malfunction or system failure. Another feature of the converter is the external programming, which sets the maximum output current by a signal provided by an external power supply. Table 6 summarizes electrical characteristics of the powertrain at locations indicated in figure 40.

For the end-to-end system demonstration, the SAFE–30 core is assembled in its modular manner and consists of two heating zones, each powered by a separate power supply. Zone 1 encompasses three modules containing heat pipes (modules 1–3 in fig. 9). There are three strings of heaters wired in parallel where each string contains four heaters in series. These twelve heaters are powered by a Hewlett Packard power supply providing 100 A at 100 Vdc. The remaining nine modules comprise zone 2 which is provided with heating power by a 400-A, 200-Vdc Linde power supply. A module in this zone has four stainless steel tubes welded to a blanked-off pipe of the same dimensions as the heat pipe. The heaters are wired in 18 parallel strings where each string contains two heaters in series.

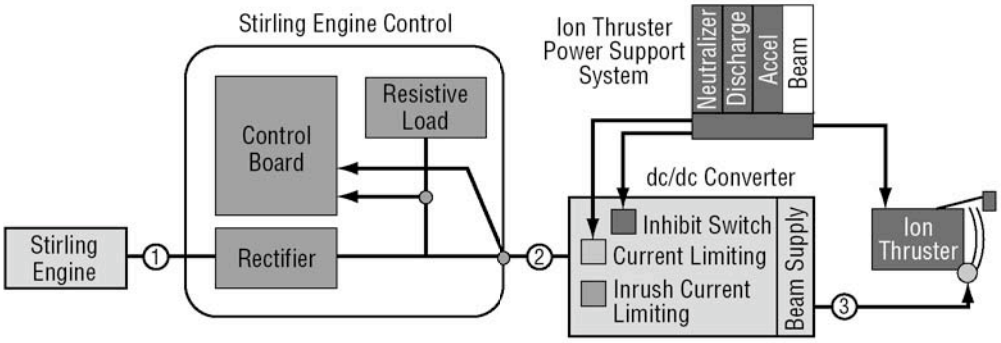

Figure 40. Schematic of the powertrain providing beam power to the ion thruster from the Stirling engine.

Table 6. Expected electrical characteristics at selected locations of the powertrain.

Location	1	2	3
Voltage	170 Vac	123 Vdc	1,000 Vdc
Current	2 A	2.9 A	300 mA
Power	350 W	350 W	300 W

4.2 Ion Thruster

Ion thrusters have been developed and tested since the 1950s, accumulating an extensive laboratory and flight history. They electrostatically accelerate positively charge particles at continuous, low to moderate power levels. The end-to-end system demonstration uses the 15-cm, C-C grid ion engine designed for a maximum input power to the power processing unit of 1.25 kW_e. Performance characteristics with C-based grid materials are comparable, although in general performance, values are slightly lower. However, C-based grids supersede with extremely low erosion rate and superior sputter resistance. These properties are key to significantly extending the lifetime of ion thrusters. Preliminary performance evaluation for Mo and graphite grids indicates a total thruster efficiency of about 52 to 66 percent with an uncertainty of up to 10 percent. Figure 41 shows the 15-cm, slotted C-C grid ion thruster as it is mounted to the door of the vacuum chamber at the JPL facilities.

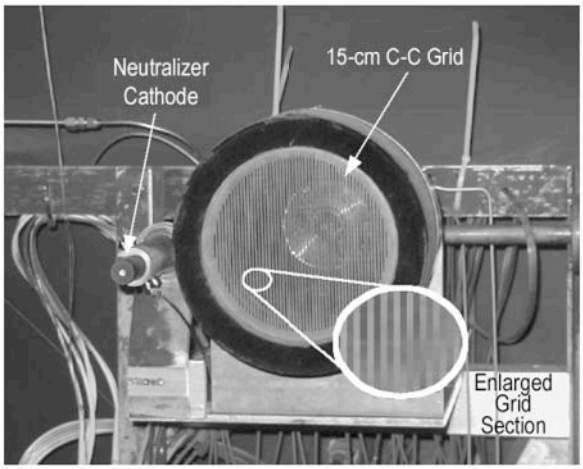

Figure 41. 15-cm, C-C grid ion thruster.

During normal operation of ion thrusters, the thruster will recycle to clear apparent shorts in the accelerator system. During a recycle event, the high voltage is turned off, the discharge current is throttled back to decrease ion production, the high voltage is turned back on, and the discharge current is returned to its normal operating point. During a recycle event, the Stirling engine and dc/dc converter system must redirect the power normally going to the thruster to a resistive load during the high voltage off time and then redirect the power back to the thruster when required. Therefore, the controller for the Stirling engine and dc/dc converter must respond faster than the controller of the ion engine.

Ion thrusters are characterized by continuous, low to moderate power level operation while electrostatically accelerating positively charged particles, such as atomic/molecular ions and colloidal particles. The characterization of electrostatic systems is based on the production mechanisms of charged particles; these can be summarized as electron bombardment, RF ionization, contact/surface and field emission ionization. The main components of a Kaufman-type ion thruster are a discharge chamber containing the magnet system and electron emitter (hollow cathode), optics/acceleration grids, neutralizer hollow cathode, and power supplies for each subsystem. Figure 42 illustrates a schematic of such a thruster whose ion source is based on electron bombardment. The hollow cathode produces and emits electrons into the discharge cavity of the thruster. These primary electrons drift towards the anode, transversing a weak axial magnetic field, which causes a spiral motion. The electrons collide and ionize neutral atoms injected into the discharge chamber. The magnetic field prevents premature losses of primary electrons to the anode and ion losses to thruster walls. The electron kinetic energy and the diameter of the discharge chamber determine the strength of the magnetic field, which can be provided by either a permanent magnet or electromagnet. The high electrostatic potential established between the plasma and the acceleration grid extracts and accelerates ions. A cathode at the exit plane of the thruster emits electrons to neutralize the ion beam. It is crucial for the operation of this thruster to keep the net charge of the beam zero. The thrust and specific impulse depend on net acceleration potential, mass-to-charge ratio of the ion, and the ion density.

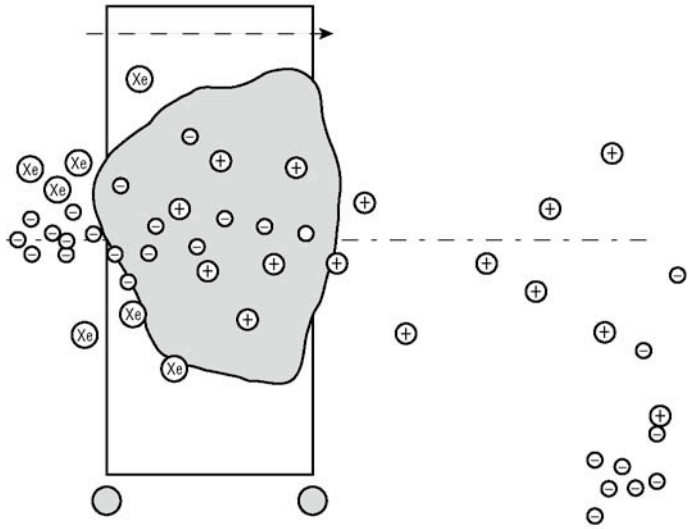

Figure 42. Schematic of ion thruster.

The 15-cm ion engine thruster can be safely operated at a beam power as low as 200 W. Figure 43 illustrates a typical trend for specific impulse and thrust as a function of power input operating with Mo grids at a constant beam current of 500 mA.

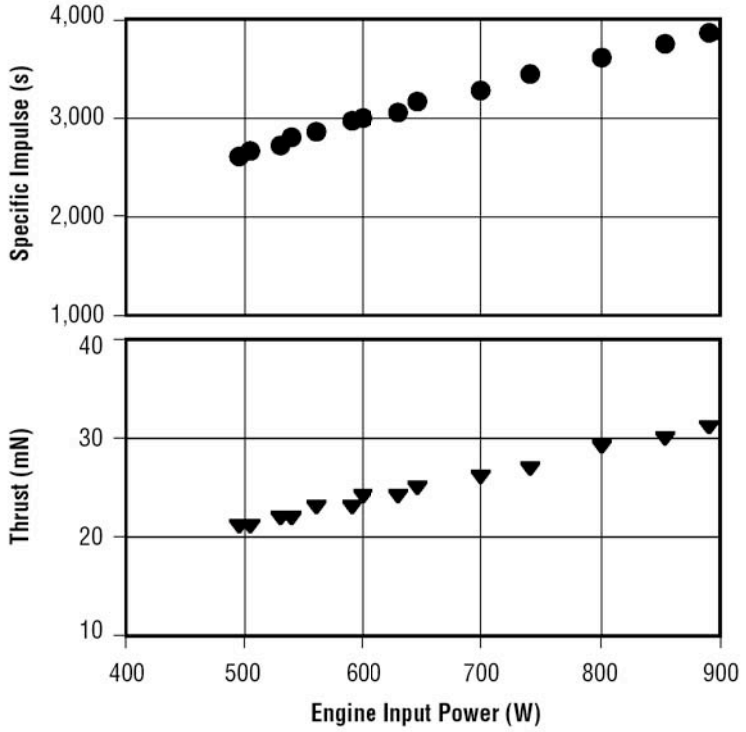

Figure 43. Specific impulse and thrust as a function of input power (data extracted with permission from Brophy, 1993).

4.3 Power Conversion System

The power conversion system converts thermal energy into usable electric power. The three main elements of this system are a heat exchanger, Stirling engine, and a dc/dc converter. The heat exchanger transfers heat from the heat pipes to the heater head of the Stirling engine. The Stirling engine then converts the thermal energy into electric power, while the dc/dc converter steps up the output voltage of the Stirling engine to the operating voltage of the ion thruster.

4.3.1 Heat Exchanger

The heat exchanger must take into account the thermal interface at the heat pipes and the heater head. Two heat exchangers were fabricated out of Cu. The main objectives of the different designs were to explore thermal flux and assembly/disassembly efficiency. Figures 44 and 45 highlight the different attachments around the heater head. Heat exchanger design 1 (HED–1) consists of three Cu pieces that clamp around the heater head and heat pipes. Stainless steel clamps provided a uniform force during high-temperature operation, since the thermal expansion of stainless steel is much smaller than Cu. The second design (HED–2) consists of two parts. The first part attaches to the heat pipes, while the

second part clamps around the heater head. Four cylinder sections are placed around the heater head and the stub, while two sets of stainless steel clamps fasten around the whole assembly. Both designs used 0.127-mm-thick Grafoil® flexible graphite for all interfaces between heater head and heat exchanger. Compressing the Grafoil ensured maximum heat transfer and prevented voids from forming, which could occur due to material expansion at high-temperature operation.

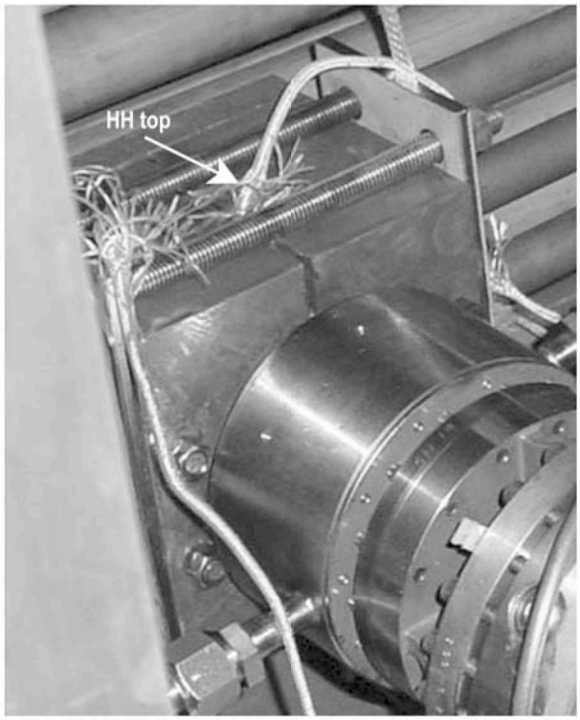

Figure 44. Heat exchanger design 1.

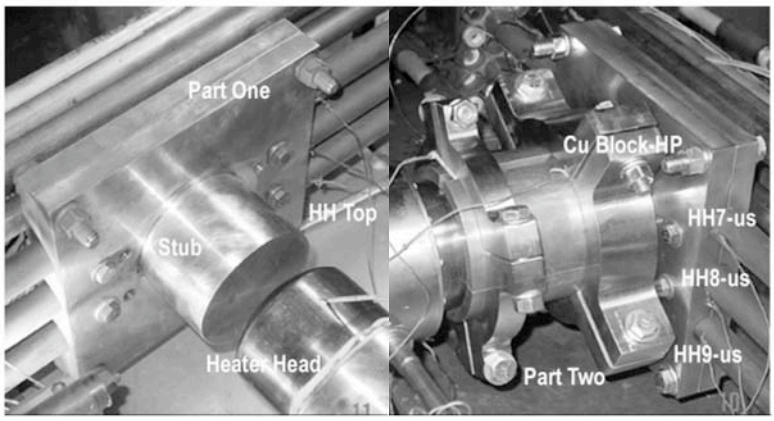

Figure 45. Parts 1 and 2 of heat exchanger design 2 and location of thermocouples.

4.3.2 Stirling Engine

The Stirling engine, an off-the-shelf device, converts thermal energy into electric energy based on the thermodynamic process described by the Stirling cycle. This engine is based on the free-piston power conversion concept using thermal-mechanical oscillations to drive a linear alternator. The active heat exchange zone on the heater head is ≈4.5 cm wide, operating at a nominal temperature of 650 °C. The heat exchanger clamps precisely over that region to ensure proper heat input to the heater head of the Stirling engine. The Stirling engine is equipped with a balance motor compensating for vibrations generated by the engine during the entire operation sequence—initial startup, power generation, and shutdown. The working fluid of the engine is He at a pressure of 45 to 52 bar, while the alternator generates 350 W at 175 Vac. The Stirling engine controller processes the generated power and provides logistics to the Stirling engine depending on operating conditions and power demand (load). The control board algorithm manages the proper loading of the Stirling engine. Sensing circuitry monitors power demand at the output, and accordingly, the control board ties in or removes stages of a resistive load array. The ac power generated by the Stirling engine is processed by rectifier circuitry and converted to an output of ≈123 Vdc and 3 A. Thermocouples on the top and the bottom of the heater head monitor the temperature during operation. Figure 46 shows the Stirling engine mounted to the heat exchanger. A fiberglass/aluminum foil blanket thermally insolates the heat exchanger.

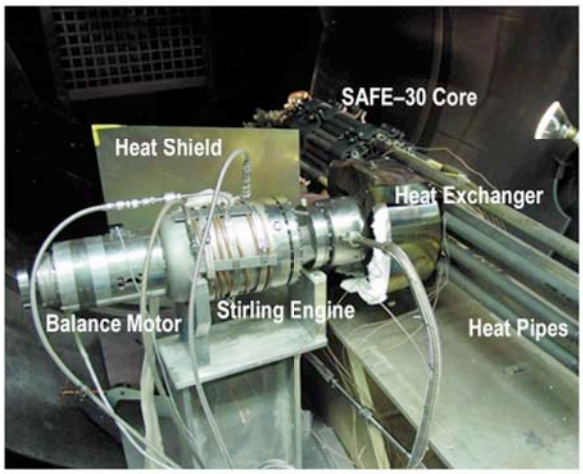

Figure 46. Stirling engine mounted to heat pipes.

4.3.3 Dc/dc Converter

The power support system for the ion thruster consists of four separate power supplies providing power to the subsystems of the thruster. However, the power generated by the Stirling engine replaces the conventional beam supply. All other subsystems of the thruster will be maintained and controlled by the power support system as depicted in the block diagram of figure 47. The dc/dc converter conditions the power for the beam supply of the ion thruster. The major functions of this device are voltage step-up, current and inrush current limitation, and power enable/inhibit control. The dc/dc converter steps up the input voltage of ≈123 Vdc to 1,000 Vdc with appropriate transformer circuitry. In addition, the device limits the inrush current during the startup sequence of the ion thruster. Without appropriate protection circuitry during this period, the current drawn by the system could be very high, damaging all crucial

components of the powertrain. This circuit, consisting of an insulated gate bipolar transistor (IGBT) and capacitor array, monitors the input current to the converter. In case the rate of rise is too high, the IGBTs are switched on and off at high frequency, allowing the capacitor bank to charge in increments using the current drawn during the pulses. The inhibit switch is another important part of the converter, which is controlled by the power support system of the ion thruster. The switch terminates the high voltage provided by the converter to the thruster in case of malfunction or system failure. The power support system provides a signal of 5 Vdc to engage the inhibit mode of the switch and a 0-Vdc signal to disengage the mode. Another feature of the converter is the external programming, which sets the maximum output current by a signal provided by an external power supply. The input signal is between 0 and 5 V, where the output current is 0 A at 0 V and 500 mA at 5 V. Any desired output current within this limit follows a linear relationship, depending on the input voltage. The dc/dc converter is rated for a power input of 500 W and its efficiency is ≈90 percent.

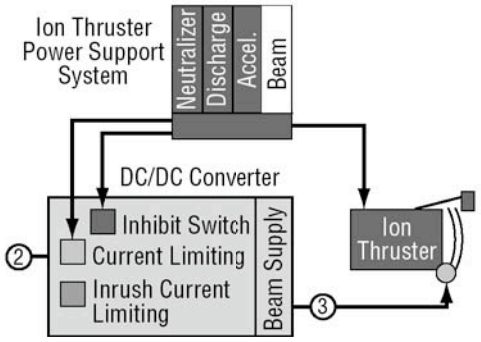

Figure 47. Block diagram of dc/dc converter and power support system of ion thruster.

4.4 Results

The end-to-end system demonstrator was operated and tested successfully at the JPL facilities. All components were successfully integrated, including the SAFE–30 core, heat pipes, heat exchanger, Stirling engine, dc/dc converter, and ion thruster. Modification reviews with the manufacturers, subsystem testing, and a phased integration approach of major components resolved thermal, electrical, and structural issues. Using Grafoil solved thermal conduction problems at the main heat exchange interfaces when operating at high temperature and in vacuum. Thermal conductivity between heater head and heat exchanger is crucial for the operation of the Stirling engine, especially for high-power operation. Modifying and adjusting the control circuitry of the dc/dc converter addressed electrical issues necessary to operate an ion thruster. In addition, the control logistics of the Stirling engine was adjusted to properly account for the fast response times required by the recycle events of ion thruster operation. This ensured flawless operation of the ion thruster and the Stirling engine during thruster startup sequence, recycle event, and zero power demand. Employing a balance motor addressed vibration and damping problems, thus minimizing any material fatigue issues which might result in a dynamic system.

Overall, the end-to-end system demonstrator performed well in all the tests and no significant problems occurred. The beam power of the thruster ranged between 50 and 150 W. Thrust measurement was not available at the facility where the end-to-end system demonstrator was installed. In the final phase of the test program, a simulated load substituted the thruster, since the thruster entered an unrelated test project and was not available for further testing. Figures 48 and 49 depict the performance of the two heat exchanger designs. Both diagrams show the power generated by the Stirling engine (Stirling power) as a function of the electrical power (core power) provided to the SAFE–30 core. In addition, they also show the temperatures of the heat pipe, the heat exchanger (Cu block), and heater head as a function of core power. The electrical power to the heaters was reduced, keeping the experiment at lower temperatures during breaks (gray shaded area). HED–1 provides a higher heat flux when compared to HED–2, since the temperature of the heat pipes, the heat exchanger, and the heater head are within ≈10 percent of each other. The temperature drop for HED–2, which occurs between the heat pipes and the heater head, is ≈30 percent. A significant higher power input to the core is needed to achieve the same power output of the Stirling engine. The relative thin profile of the cylinder sections of HED–2 significantly reduces heat conductivity. A significant advantage of HED–2 over HED–1 is the installation of the heat exchanger.

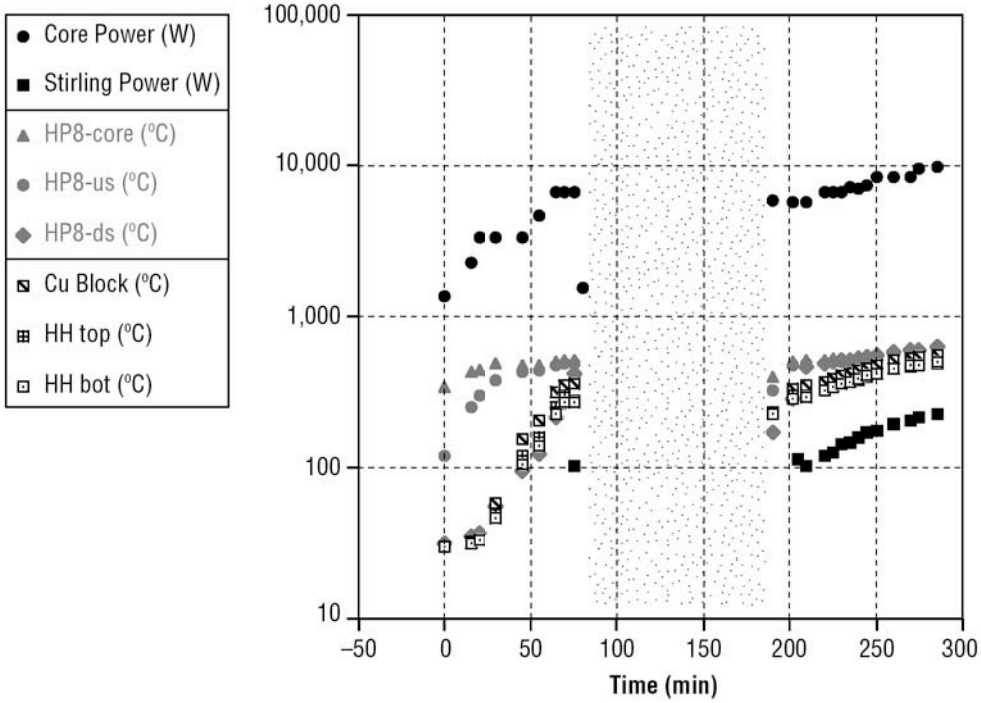

Figure 48. HED–1: Stirling power and temperature at key components as a function of electrical power provided to SAFE–30 core.

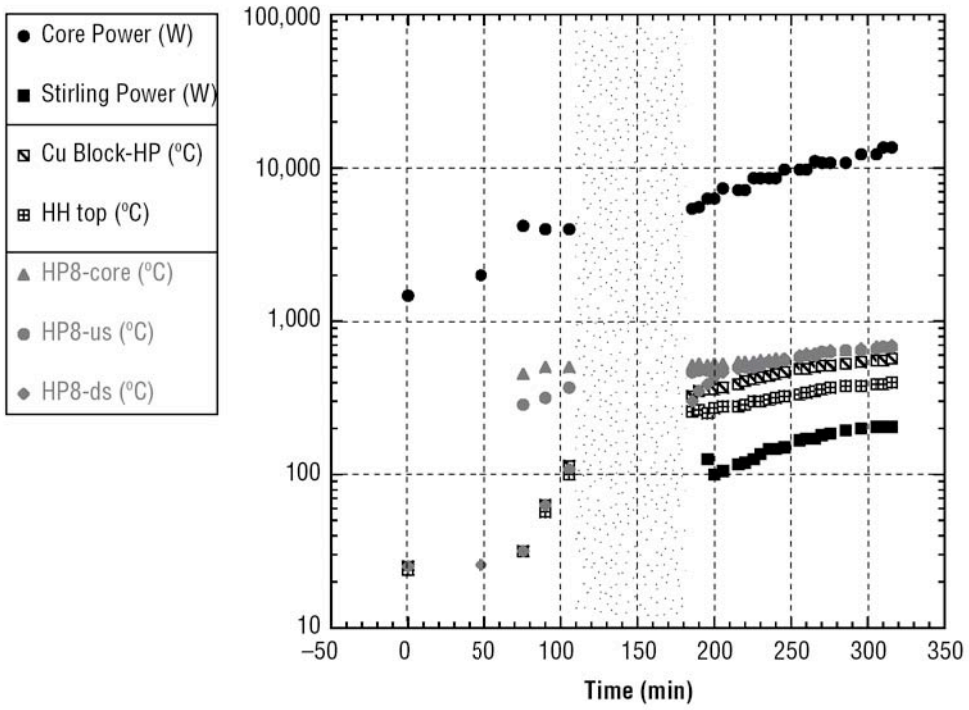

Figure 49. HED–2: Stirling power and temperature at key components as a function of electrical power provided to SAFE–30 core.

5. CONCLUSIONS

High confidence in fission system performance can be attained through a series of nonnuclear tests. In order to maximize the benefits of a strong nonnuclear testing program, tangible realistic prototypic hardware milestones can be shown on a yearly basis. This program demonstrates that each product can build on the success of its predecessor and can be applicable to the next system. The MUTT successfully demonstrated the use of resistance heaters to realistically simulate heat from fission, the ability to use several different instrumentation techniques for measuring temperature and pressure in a simulated fission (thermal hydraulic) environment, and the energy transfer capability and operation of a heat pipe under worst-case operating conditions (fast startup and exposure to air). Because the heat transfer within the SAFE–30 system is highly predictable, the SAFE–30 and SAFE–30 end-to-end demonstrator test programs provided experimental data to anchor computational models, which predicted the temperature and heat transfer within the core along the heat pipes and into the energy conversion cycle. It was also used to explore the operational constraints for such a system. These data were used as a research tool supporting the development of a larger; e.g., 100-kW, core design.

The SAFE–30 tests provide an overview of the general techniques, environments, and hardware used to simulate the heat transfer within a nuclear core. The later tests, which implemented the Stirling engine, were completed to demonstrate that an HPS is a realistic concept that can provide power for future space applications. A primary goal was to demonstrate the use of a heat transfer computer model to reliably predict the operations of a system, such as SAFE–30 resistance heater tests. The initial results indicate that the model was able to predict behavior, even with less-than-textbook test conditions, demonstrating the overall capability of the program. In general, the tests indicate that the SAFE system is a robust, near-term, low-cost simple system that works. Last, the SAFE–30 resistance heater tests were one successful step along a path that promises to bring mankind closer to the ultimate goal of understanding and routinely exploring the depths of outer space.

Key technical contributors to the MUTT and SAFE–30 testing programs are listed in the appendix.

APPENDIX— KEY TECHNICAL CONTRIBUTORS TO THE MODULE UNFUELED THERMOHYDRAULIC TEST AND SAFE, AFFORDABLE 30-kW FISSION ENGINE TESTING PROGRAMS

Contributors from LANL include:

Dave Poston
Bob Reid
Tom Sena
Rick Kapernick
Gordon Wilcutt
Lee Van Duyn (Purdue Student)
Laurie Hixson
Herb Funston
Jim Lee

Contributors from Sandia National Laboratory include:

Ron Lipinski
Steve Wright
Roger Leonard

Contributors from MSFC include:

Mike Houts
Melissa Van Dyke
Ricky Dickens
Tom Godfroy
Ivana Hrbud
Jim Martin
Pat Salvail

Contributors from JPL include:

Keith Goodfellow
Jay Polk

Contributors from Glenn Research Center include:

Dick Shaltens
Jeff Schrieber
Lee Mason

BIBLIOGRAPHY

Allen, D.M.; Bennett, G.L.; El-Genk, M.S.; Newhouse, A.R.; and Rose, M.F.: "Maintenance of the U.S. Space Nuclear Power Program: An AIAA Position Paper," in *Proceedings of the 46th International Astronautical Congress*, IAF–95–R.1.05, Oslo, Norway, October 1995.

ASM Handbook, Volume 02: Properties and Selection: Nonferrous Alloys and Special-Purpose Materials, American Society for Metals International, Materials Park, OH, 1991.

ASM Handbook, Volume 06: *Welding, Brazing, and Soldering*, Davis, J.; Ferjutz, K.; and Wheaton, N. (eds.), American Society for Metals International, Materials Park, OH, 1993.

ASM Handbook, Volume 20: *Materials Selection and Design*, Dieter, G. (ed.), American Society for Metals International, Materials Park, OH, 1997.

Baxter, W.F.; Burchell, G.P.; Fitzgibbon, D.G.; and Swita, W.R.: "SP–100 Ground Engineering System Test Site Description and Progress Update," in *Proceedings of Space Nuclear Power and Propulsion Department of Energy Conference,* No. 910116, American Institute of Physics, New York, NY, pp. 1329–1334, 1991.

Borowski, S.K.; Dudzinski, L.A.; and McGuire, M.L.: "Vehicle and Mission Design Options for the Human Exploration of Mars/Phobos Using Bimodal NTR and LANTR Propulsion," *NASA/TM—1998–208834*, Glenn Research Center, Cleveland, OH, December 1998.

Brophy, J.R.; Pless, L.C.; Mueller, J.; and Anderson, J.R.: "Operating Characteristics of a 15-cm-Diameter Ion Engine for Small Planetary Spacecraft," in *Proceedings of 23d International Electric Propulsion Conference*, Paper No. IEPC–93–110, Seattle, WA, September 1993.

Carlson, W.F.; and Bitten, E.J.: "A Facility for Testing 10 to 100-kW_e Space Power Reactors," in *Proceedings of Space Nuclear Power and Propulsion Conference*, No. 271, American Institute of Physics New York, NY, pp. 867–872, 1993.

Chang-Diaz, F.R.; Braden, E.; Johnson, I.; et al.: "Rapid Mars Transits with Exhaust-Modulated Plasma Propulsion," NASA Technical Paper 3539, Johnson Space Center, Houston, TX, March 1995.

Cybulski, J.R.; Shellhammer, D.M.; Lovell, R.R.; Domino, E.J.; and Kotnik, J.T.: "Results from SERT I Ion Rocket Flight Test," NASA Technical Note D–2718, 1965.

Dailey, C.L.; and Lovberg, R.H.: "The PIT Mk V Pulsed Inductive Thruster," *NASA CR–191155*, Lewis Research Center, Cleveland, OH, July 1993.

Fallas, T.T.; Gluck, R.; Motwani, K.; Clay, H.; and O'Neill, G: "SP–100 Nuclear Assembly Test Assembly Functional Requirements and System Arrangement," in *Proceedings of Space Nuclear Power and Propulsion Department of Energy Conference*, No. 910116, American Institute of Physics, New York, NY, pp. 1,323–1,328, 1991.

Gubareff, G.G.; Janssen, J.E.; and Torborg, R.H.: *Thermal Radiation Properties Survey*, Honeywell Research Center, Minneapolis, MN, 1960.

Houts, M.; Van Dyke, M.; Godfroy, T.; et al.: "A Three Phase Approach to the Development of Space Fission Propulsion Systems," in *Proceedings of Space Technology and Applications International Forum 2001 Conference*, American Institute of Physics, New York, NY, 2001.

Koenig, D.R.: Experience Gained from the Space Nuclear Rocket Program (Rover), *LA–10062–H*, Los Alamos National Laboratory, Los Alamos, NM, 1986.

LaPointe, M.R.; and Sankovic, J.M.: "High Power Electromagnetic Propulsion at the NASA Glenn Research Center," in *Proceedings of Space Technology and International Forum 2000 Conference*, No. 504, American Institute of Physics, New York, NY, pp. 1538–1543, January 2000.

Mueller, J.; Brown, D.K.; Garner, C.E.; and Brophy, J.R.: "Fabrication of Carbon-Carbon Grids for Ion Optics," in *Proceedings of International Electric Propulsion Conference*, IEPC–93–112, Seattle, WA, September 1993.

Mueller, J.M.; Brophy, J.R.; Brown, D.K.; and Garner, C.E.: "Performance Characterization of 15-cm Carbon-Carbon Composite Grids," in *Proceedings of 30th AIAA Joint Propulsion Conference*, AIAA–94–3118, Indianapolis, IN, June 1994.

Pederson, K.; et al.: "Results of 30 kWt Safe Affordable Fission Engine (SAFE-30) Primary Heat Transport Testing," in *Proceedings of Space Technology and Applications International Forum 2001 Conference*, No. 552, American Institute of Physics, New York, NY, pp. 843–848, 2001.

Polk, J.; Tikhonov, V.; and Semenikhin, S.: "200-kW Lithium-Fed Thruster Development and Preliminary Test," in *Proceedings of 35th AIAA Joint Propulsion Conference*, Paper No. AIAA–99–2285, Los Angeles, CA, June 1999.

Poston, D.I.; Voit, S.L.; Reid, R.S.; and Ring, P.J.: "The Heat pipe Power System (HPS) for Mars Outpost and Manned Mars Missions," in *Proceedings of Space Technology and Applications International Forum 2000 Conference*, No. 504, pp. 1327–1334, 2000.

Reid, R.S.; Sena, J.T.; and Merrigan, M.A.: "Transient Tests of a Molybdenum-Lithium Heat Pipe," in *Proceedings of 11th International Heat Pipe Conference*, Tokyo, Japan, September 12–16, 1999.
Reid, R.S.; Sena, J.T.; Merrigan, M.A.; et al.: "Heat Pipe Development for Advanced Energy Transport Concepts," *LA–13549–PR*, Los Alamos National Laboratory, Los Alamos, NM, 1999.

Sackheim, R.; et al.: "In-Space Nuclear Power as an Enabling Technology for Deep Space Exploration," in *Proceedings of 36th AIAA/ASME/SAE/ASEE Joint Propulsion Conference*, AIAA–2000–3881, Reston, VA, 2000.

Sankovic, J.; Oleson, S; and LaPointe, M.: "NASA GRC Activities in High Power Electric Propulsion," *Proceedings of NASA Jet Propulsion Laboratory 10th Advanced Space Propulsion Workshop*, pp. 665–681, April 1999.

Schmidt, G.R.: "Propulsion Research and Technology at NASA Marshall Space Flight Center," in *Proceedings of 34th AIAA Joint Propulsion Conference*, AIAA–98–3230, Cleveland, OH, July 1998.

Schreiber, J.: "Tutorial on Free-Piston Stirling Power Conversion Technology—How Does It Work?" in *Proceedings of Space Technology and Applications International Forum 2001 Conference*, No. 552, Albuquerque, NM, February 2001.

Schwartz, M.: *Brazing*, American Society for Metals International, Materials Park, OH, 1990.

Van Dyke, M.K.; Godfroy, T.; Houts, M.; et al.: "Results of a First Generation Least Expensive Approach to Fission Module Tests: Non-Nuclear Testing of a Fission System," in *Proceedings of Space Technology and International Forum 2000 Conference*, No. 504, pp. 1,211–1,217, January 2000.

Van Dyke, M.; Houts, M.; Pedersen, K.; et al.: "Phase I Space Fission Propulsion System Testing and Development Progress," in *Proceedings of 36th AIAA/ASME/SAE/ASEE Joint Propulsion Conference*, AIAA–2000–5356, Reston, VA, 2000.

Van Dyke, M.K.; Houts, M.; Pederson, K.; et al.: "Phase 1 Space Fission Propulsion System Testing and Development Progress," in *Proceedings of Space Technology and International Forum 2001 Conference*, 552, Albuquerque, NM, pp. 837–842, February 2001.

Watson, C.W.: "Nuclear Rockets: High-Performance Propulsion for Mars," *LA–12784–MS*, Los Alamos National Laboratory, Los Alamos, NM, May 1994.

Woloshun, K.A.; Merrigan, M.A.; and Best, E.D: "HTPIPE: A Steady-State Heat Pipe Analysis Program," *LA–11324–M*, Los Alamos National Laboratory, Los Alamos, NM, 1988.

REPORT DOCUMENTATION PAGE

Form Approved
OMB No. 0704-0188

1. AGENCY USE ONLY *(Leave Blank)*	2. REPORT DATE	3. REPORT TYPE AND DATES COVERED
	November 2003	Technical Memorandum

4. TITLE AND SUBTITLE

Overview of Nonnuclear Testing of the Safe, Affordable 30-kW Fission Engine, Including End-to-End Demonstrator Testing

5. FUNDING NUMBERS

6. AUTHORS

M.K. Van Dyke, J.J. Martin, and M.G. Houts

7. PERFORMING ORGANIZATION NAMES(S) AND ADDRESS(ES)

George C. Marshall Space Flight Center
Marshall Space Flight Center, AL 35812

8. PERFORMING ORGANIZATION REPORT NUMBER

M–1095

9. SPONSORING/MONITORING AGENCY NAME(S) AND ADDRESS(ES)

National Aeronautics and Space Administration
Washington, DC 20546–0001

10. SPONSORING/MONITORING AGENCY REPORT NUMBER

NASA/TM—2003–212930

11. SUPPLEMENTARY NOTES

Prepared by the Propulsion Research Center, Space Transportation Directorate

12a. DISTRIBUTION/AVAILABILITY STATEMENT

Unclassified-Unlimited
Subject Category 20
Available: NASA CASI (301)621–0390

12b. DISTRIBUTION CODE

13. ABSTRACT *(Maximum 200 words)*

Successful development of space fission systems will require an extensive program of affordable and realistic testing. In addition to tests related to design/development of the fission system, realistic testing of the actual flight unit must also be performed. At the power levels under consideration (3–300 kW electric power), almost all technical issues are thermal or stress related and will not be strongly affected by the radiation environment. These issues can be resolved more thoroughly, less expensively, and in a more timely fashion with nonnuclear testing, provided it is prototypic of the system in question. This approach was used for the safe, affordable fission engine test article development program and accomplished via cooperative efforts with Department of Energy labs, industry, universities, and other NASA Centers. This Technical Memorandum covers the analysis, testing, and data reduction of a 30-kW simulated reactor as well as an end-to-end demonstrator, including a power conversion system and an electric propulsion engine, the first of its kind in the United States.

14. SUBJECT TERMS

fission, simulated nuclear testing, nuclear electric propulsion, power conversion, heat pipe, testing, Stirling engine, end-to-end demonstrator

15. NUMBER OF PAGES

80

16. PRICE CODE

17. SECURITY CLASSIFICATION OF REPORT	18. SECURITY CLASSIFICATION OF THIS PAGE	19. SECURITY CLASSIFICATION OF ABSTRACT	20. LIMITATION OF ABSTRACT
Unclassified	Unclassified	Unclassified	Unlimited